

Integrated Sachs Wolfe Effect and Rees Sciama Effect

Atsushi J. Nishizawa¹

¹ *Kavli Institute for the Physics and Mathematics of the Universe (Kavli IPMU, WPI), The University of Tokyo, Chiba 277-8582, Japan*

**E-mail: atsushi.nishizawa@ipmu.jp*

.....
It has been around fifty years since R. K. Sachs and A. M. Wolfe predicted the existence of anisotropy in the Cosmic Microwave Background (CMB) and ten years since the integrated Sachs Wolfe effect (ISW) was first detected observationally. The ISW effect provides us with a unique probe of the accelerating expansion of the Universe. The cross-correlation between the large-scale structure and CMB has been the most promising way to extract the ISW effect from the data. In this article, we review the physics of the ISW effect and summarize recent observational results and interpretations.
.....

Subject Index Cosmological perturbation theory, Cosmic background radiations, Dark energy and dark matter

1. Overview

After the discovery of the isotropic radiation of the Cosmic Microwave Background (CMB) of the Universe by A. A. Penzias and R. W. Wilson in 1965 [100], R. K. Sachs and A. M. Wolfe predict the existence of anisotropy in the CMB associated with the gravitational redshift in 1967 [116]. They fully integrate the geodesic equation in a perturbed Friedman-Robertson-Walker (FRW) metric in the fully general relativistic framework. The Sachs-Wolfe (SW) is the first paper that predicts the presence of the anisotropy in the CMB which now plays an important role for constraining cosmological models, the nature of dark energy, modified gravity, and non-Gaussianity of the primordial fluctuation.

Let us begin by reviewing the history. In the first twenty years since the Sachs-Wolfe paper, most of the works were focused on the extension of the Sachs-Wolfe calculation to non-linear collapsed object [96, 113], or non-standard cosmological model such as topological defects [66]. Partridge and Wilkinson 1967 first gave a glimpse of the existence of inhomogeneity in the CMB temperature by using the Dicke Radiometer [143]. They found the temperature excess on the direction of the known quasar cluster position and considered it as the Rees-Sciama effect [113]. In the age of the COBE satellite, the Sachs-Wolfe paper attracted a huge attention. Most of the papers were focused on the theoretical prediction that was related to the observation; prediction of the amplitude of the quadrupole power for the SW effect. [17, 46–48]. Crittenden & Turok 1996 pointed out that the gravitational potential may decay in the Λ dominated Universe at $z < 1$ to produce the ISW signal [24]. They also proposed a novel method to detect the ISW effect by cross correlating the large-scale structure with the CMB. Kneissl et al. 1997 made an attempt to extract the ISW effect by cross correlating the CMB observed by the COBE with the ROSAT X-ray background [68], Boughn & Crittenden 2002 used the NVSS radio galaxies for the cross correlation [11], and Boughn et al. 1998

used the HEAO1 A2 X-ray background [14] but none of them could find the significant detection. The Sachs-Wolfe paper has attracted a renewed attention in the WMAP era. The first detection of the ISW was finally achieved by cross-correlating the WMAP first-year data with the number count of radio galaxies from the NVSS data, as well as with the HEAO1 A1 X-ray data [12]. Subsequently a lot of detections with various mass tracers have been reported. In the early 2000's, much work was focused on obtaining cosmological constraint on dark energy models from the ISW effect, while in the late 2000's to present, more and more works studied various systematic effects which may enter in different ways for different measurement methods.

In this paper, we review the ISW effect from theoretical derivation of the basic equations to the present cosmological interpretations. The paper is organized as follows. In section 2, we revisit the derivation of the CMB anisotropy induced by the perturbation of the background geometry decomposed into scalar, vector and tensor modes. In section 3, we discuss the statistical properties of the ISW effect and the method to measure it in the cross correlation with the large-scale structure. We also discuss the possible systematic effects that affect our interpretations. In section 4, we provide cosmological applications of the ISW effect including constraints on dark energy and primordial non-Gaussianity. In section 5, we give a summary.

2. Theory of the ISW effect In the Standard Cosmology

In this section, we derive the basic equations of the ISW effect based on the original paper [116]. We first write the line element in a spatially flat FRW metric,

$$ds^2 = g_{\mu\nu} dx^\mu dx^\nu = a^2(\tau) \tilde{g}_{\mu\nu} dx^\mu dx^\nu, \quad (1)$$

where a is the scale factor that depends solely on the conformal time τ and $g_{\mu\nu}$ and $\tilde{g}_{\mu\nu}$ are the metric and a conformally transformed metric, respectively. The metric consists of perturbed and unperturbed parts, i.e. $\tilde{g}_{\mu\nu} = \eta_{\mu\nu} + \tilde{h}_{\mu\nu}$, with the unperturbed metric $\eta_{\mu\nu} = \text{diag}(-, +, +, +)$ and $\tilde{h}_{\mu\nu} \ll 1$. Here we ignore all the quantity of order $\mathcal{O}(h^2)$ and higher. Introducing two affine parameters τ and λ to characterize the photon geodesic in the $g_{\mu\nu}$ and $\tilde{g}_{\mu\nu}$ metric respectively, we have $d\tau = a^2 d\lambda$ since the action of the geodesic should be invariant under the rescaling of $g_{\mu\nu} \rightarrow a^2 g_{\mu\nu}$ and $d\tau \rightarrow a^2 d\lambda$. To simplify the calculation, we first work on the $\tilde{g}_{\mu\nu}$ system and then translate it to the $g_{\mu\nu}$ system.

The metric perturbation can be decomposed into scalar, vector and tensor modes. h_{0i} can be divided into the contributions from scalar and vector while h_{ij} can be divided into the contributions from scalar, vector, and tensor modes as,

$$\tilde{h}_{00} = -2A^{(s)} \quad (2)$$

$$\tilde{h}_{0i} = -\partial_i B^{(s)} - B_i^{(v)} \quad (3)$$

$$\tilde{h}_{ij} = -2 \left[D^{(s)} \delta_{ij} - \left(\partial_i \partial_j - \frac{1}{3} \nabla^2 \right) C^{(s)} \right] + (\partial_j C_i^{(v)} + \partial_i C_j^{(v)}) + C_{ij}^{(t)}, \quad (4)$$

where A, B, C and D are arbitrary functions and superscript with the parenthesis (s), (v) and (t) stand for the scalar, vector and tensor quantities respectively. The derivative ∂_i denotes the 3 dimensional covariant derivative. The scalar perturbation is not generated from the vector or tensor mode and the vector perturbation is not generated from the tensor mode thus we have constraints as

$$\partial^i B_i^{(v)} = 0, \quad (5)$$

$$\partial^i C_i^{(v)} = 0, \quad C_i^{(t)i} = 0, \quad \partial^i C_{ij}^{(t)} = 0. \quad (6)$$

2.1. Scalar mode Linear Perturbation

We now need to fix a gauge degree of freedom. For the scalar perturbation, the conformal Newtonian gauge (longitudinal gauge) is useful [e.g. 78, 87]. In the Newtonian gauge, all the gauge degrees of freedom are used to eliminate the off-diagonal components of the perturbed metric. Then the variables are fixed as $B^{(s)} = C^{(s)} = 0$, and the metric perturbation can be fully described by the two scalar quantities of $A = \Phi$, $D = \Psi$ which are already gauge invariant. The metric turns out to be

$$ds^2 = a^2[-(1 + 2\Phi)d\tau + (1 - 2\Psi)\delta_{ij}dx^i dx^j], \quad (7)$$

where Φ and Ψ are Newtonian potential and curvature perturbation respectively. Then we naturally obtain the non vanishing connections,

$$\tilde{\Gamma}_{00}^0 = \Phi', \quad \tilde{\Gamma}_{0i}^0 = \partial_i \Phi, \quad \tilde{\Gamma}_{ij}^0 = -\Psi' \delta_{ij}, \quad (8)$$

where $' \equiv \partial/\partial\tau$. The photon geodesic $x(\lambda)$ can be obtained by solving the geodesic equation,

$$\frac{d\tilde{k}^\alpha}{d\lambda} = \tilde{\Gamma}_{\mu\nu}^\alpha \tilde{k}^\mu \tilde{k}^\nu, \quad (9)$$

where we introduce the 4-momentum $\tilde{k}^\mu = \frac{dx^\mu}{d\lambda}$. It can be decomposed into the unperturbed and perturbed geodesic as $\tilde{k}^\mu = \bar{k}^\mu + \delta\tilde{k}^\mu$. The photon energy is measured by the observer moving with the fluid, thus the observed energy needs to be projected with the 4-velocity in the un-tilde $g_{\mu\nu}$ system,

$$E = g_{\mu\nu} u^\mu k^\nu. \quad (10)$$

By definition $g_{\mu\nu} u^\mu u^\nu = 1$, the unperturbed component is $u^\mu = a^{-1}(1, 0, 0, 0)$. The 4-velocity is written as $u^\mu = a^{-1}(1 - \Phi, v^i)$. The spatial 3 dimensional velocity is already first order quantity, hence we do not need to explicitly solve the spacial part of the geodesic equation, (9). The solution for the unperturbed background is trivial, i.e. $\bar{k}^0 = 1, \bar{k}^i = e^i$, where $e = (1, e^i)$ is the 4-tangent vector of the geodesic. The time part of the first order solution of equation (9) is integrated as

$$\frac{\delta\tilde{k}^0}{a^2} = \frac{\delta\tilde{k}^0}{a^2} \Big|_{\tau_*} + 2[\Phi(\tau_*) - \Phi(\tau_0)] + \int_{\tau_0}^{\tau_*} (\Phi' + \Psi') d\tau, \quad (11)$$

where τ_* denotes the conformal time of the decoupling time, and τ_0 today. Now the redshift is defined by the photon energy ratio between emitter and receiver, $1 + z \equiv E(\tau_*)/E(\tau_0)$. Using the fact that under the rescaling of $\tilde{g}_{\mu\nu} \rightarrow g_{\mu\nu}$, the 4-momentum scales as $\tilde{k}^\mu \rightarrow a^2 k^\mu$,

$$1 + z = \frac{k^\mu u_\mu|_{\tau_*}}{k^\nu u_\nu|_{\tau_0}}, \quad (12)$$

Since the temperature drops with redshift as $T = T_*/(1 + z)$, using equations (10), (11) and (12), observed temperature fluctuation over the sky is

$$\frac{\delta T^{(s)}}{T} = \frac{\delta T^{(s)}}{T} \Big|_{\tau_*} - \Phi(\tau_0) + \Phi(\tau_*) + [\mathbf{v} \cdot \mathbf{e}]_{\tau_0}^{\tau_*} + \int_{\tau_0}^{\tau_*} (\Phi' + \Psi') d\tau, \quad (13)$$

apart from the isotropic temperature. The first term is the intrinsic photon fluctuation at the last scattering surface other than those induced by the metric perturbation; $\delta T/T|_{\tau_*} = \delta_\gamma(\tau_*)/4$. The second term is the gravitational redshift due to our gravitational potential which is the monopole contribution and can not be observed. The third term represents the temperature anisotropy caused by the gravitational redshift due to the potential fluctuations at the decoupling epoch, which is called

the naive or ordinary Sachs Wolfe effect in the literature. Since it also has the spacial dependence, we shall write $\Phi(\tau_*) = \Phi(\tau_*, \hat{\mathbf{n}})$ where $\hat{\mathbf{n}}$ denotes the angular position on the sky. The fourth term is the Doppler effect that is induced by the relative motion between the observer and the CMB last scattering surface. The final integral term represents the temperature anisotropy caused by the time variation of gravitational potential integrated along the line of sight, and this is the ISW effect. Since the gravitational potential is static in the matter dominated Universe, i.e. Einstein de-Sitter Universe, the ISW effect vanishes in the linear perturbation limit. Thus the ISW effect induces temperature fluctuation at radiation dominated era or dark energy or curvature dominated Universe. The former is called the early ISW and the latter the late ISW effect. We note that from the current observations the matter radiation equality time, $z_{\text{eq}} \simeq 3300$ is well before the decoupling, $z_{\text{dec}} = 1090$ and thus the temperature fluctuation of the early ISW is regarded as a part of the primary anisotropy. We also note that the careful authors include the visibility function to the last scattering surface in the integrand, $e^{-\tau}$, where τ is the optical depth; however, in the flat Λ CDM Universe, the redshift where the ISW effect becomes important is at $z < 1$, and thus $e^{-\tau} = 1$ is a good approximation.

2.2. Vector and Tensor mode Perturbations

The photon geodesic is perturbed also by the vector and tensor modes. For the vector mode, the geodesic perturbation can be characterized by B_i and C_i . The temperature anisotropy induced by the vector mode is given by

$$\frac{\delta T^{(v)}}{T} = \frac{\delta T^{(v)}}{T} \Big|_{\tau_*} + [\mathcal{V}^i e_i]_{\tau_0}^{\tau_*} + \frac{1}{2} \int_{\tau_0}^{\tau_*} d\tau (\partial_i V_j + \partial_j V_i) e^i e^j, \quad (14)$$

where the first term is intrinsic vector type temperature fluctuation, \mathcal{V}_i is a rotational component of the velocity and $V_i = C'_i + B_i$. In the standard scenario of the inflation, the vacuum fluctuation generates no super-horizon vector mode perturbation [74]. Even if it is generated with some exotic mechanisms, vector mode has a only decaying mode solution which can be negligible at later times; thus we shall assume that the vector mode does not exist [73]. In practice, it makes negligible contribution to the CMB temperature observation so we assume it is absent.

The tensor mode, in other words the gravitational wave, is given by the traceless transverse rank two tensor, C_{ij} in equation (4). The temperature fluctuation induced by the tensor mode metric perturbation is

$$\frac{\delta T^{(t)}}{T} = \frac{\delta T^{(t)}}{T} \Big|_{\tau_*} - \frac{1}{2} \int_{\tau_0}^{\tau_*} d\tau C'_{ij} e^i e^j. \quad (15)$$

The tensor mode decays on the scales smaller than the horizon at the decoupling, say ~ 1 degree, and the significant contribution comes from the largest scales. Recently, the BICEP2 experiment report that they detect a signature of large amplitude of the gravitational wave which is observed by the B-mode polarization power spectrum of the CMB [8]. This is indeed the tensor ISW effect! The best fit value of the tensor to scalar ratio is $r = 0.16$ after removing the foreground components.

2.3. Spectrum of the ISW effect

In this section, we consider the power spectrum for the scalar mode perturbation. Here we assume that the energy contents of the Universe have no anisotropic stress, which relates Φ and Ψ as $\Phi = \Psi$.

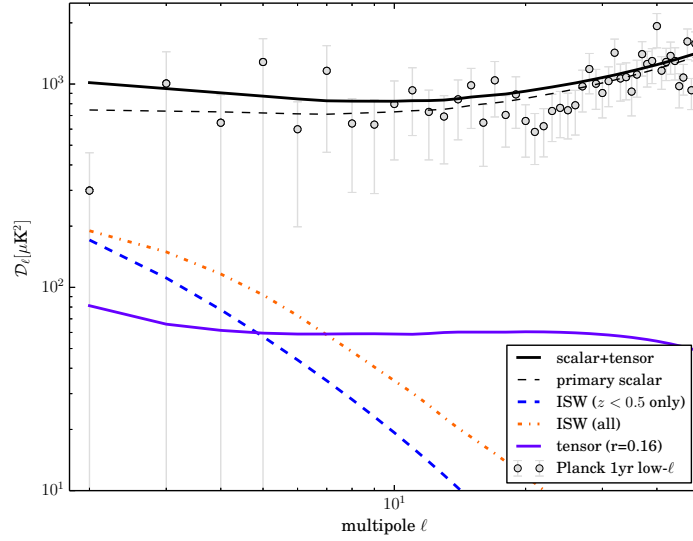


Fig. 1 Temperature anisotropy at low multipoles. The thick solid line shows the total anisotropy integrated from today to the last scattering surface including scalar and tensor contributions. The thin dashed line shows the scalar contribution of the primary anisotropy at the last scattering surface, the thick dashed and the dot-dashed lines show contributions from the ISW effect generated at $z < 0.5$ and $z < 100$, respectively and the horizontal thick purple line below $100[\mu\text{K}^2]$ shows the tensor contribution with $r = 0.16$. Also shown by points with errorbars is the CMB power spectrum obtained by the first year low- ℓ Planck data [106].

Then the integrated Sachs Wolfe effect is written as

$$\Theta_{\text{ISW}}(\hat{\mathbf{n}}) \equiv \frac{\delta T_{\text{ISW}}(\hat{\mathbf{n}})}{T} = 2 \int \frac{\partial \Phi(\hat{\mathbf{n}}r, \tau)}{\partial \tau} d\tau. \quad (16)$$

Now the potential Φ can be related to the density fluctuation through the Poisson equation. Working in the Fourier space makes things simple. In the Fourier space, the Poisson equation in the flat FRW Universe is,

$$\Phi(\mathbf{k}, \tau) = \frac{3}{2} \frac{\Omega_m}{a} \left(\frac{H_0}{k} \right)^2 \left[\frac{3aH}{k^2} \theta(\mathbf{k}, \tau) + \delta(\mathbf{k}, \tau) \right] \quad (17)$$

where δ and θ are the density contrast and divergence of velocity of the matter, respectively and Ω_m and H_0 are the matter density and Hubble parameter today, respectively. In the Newtonian limit where the scale of interest is well smaller than the horizon, i.e. $k \gg aH$, equation (17) is reduced to the well known form, $\Phi = 3\Omega_m/2a(H_0/k)^2\delta$. We usually expand the Fourier basis into the spherical harmonics and spherical Bessel function to obtain the full sky expression of the fluctuation in a direction $\hat{\mathbf{n}}$,

$$\Theta_{\text{ISW}}(\hat{\mathbf{n}}) = 12\pi\Omega_m H_0^2 \sum_{lm} (-i)^l \int d\tau \int \frac{dk d\Omega_{\hat{\mathbf{k}}}}{(2\pi)^3} \frac{\partial}{\partial \tau} \left(\frac{\delta(\mathbf{k}, \tau)}{a} \right) j_l(kr) Y_{lm}(\hat{\mathbf{n}}) Y_{lm}^*(\hat{\mathbf{k}}) \quad (18)$$

The spherical harmonic counterpart is obtained using the orthogonality of the spherical harmonics,

$$\Theta_{lm} = \int d\Omega_{\hat{\mathbf{n}}} \Theta(\hat{\mathbf{n}}) Y_{lm}^*(\hat{\mathbf{n}}) = 12\pi\Omega_m H_0^2 (-i)^l \int d\tau \int \frac{dk d\Omega_{\hat{\mathbf{k}}}}{(2\pi)^3} \frac{\partial}{\partial \tau} \left(\frac{\delta(\mathbf{k}, \tau)}{a} \right) j_l(kr) Y_{lm}^*(\hat{\mathbf{k}}). \quad (19)$$

The angular power spectrum is then calculated as,

$$C_l^{\text{ISW}} = \langle \Theta_{lm} \Theta_{lm}^* \rangle = \frac{18}{\pi} \Omega_m^2 H_0^4 \int dk P(k) \left[\int dr D(f-1) \mathcal{H} j_l(kr) \right]^2, \quad (20)$$

where f is the velocity factor, $f \equiv d \ln D / d \ln a$ and $\mathcal{H} = a' / a$ is the conformal Hubble parameter. The numerical calculation of equation (20) would be formidable because of the oscillatory behavior of the Bessel function. The Hankel or also known as Fourier-Bessel transform can be helpful instead of the direct integration [51, 97]. The Limber's approximation is used in the literature but it is accurate only up to $\sim 10\%$ on scales larger than $l < 10$ [e.g. 35].

Figure 1 shows the power spectra of the primary CMB temperature fluctuation and the ISW effect for the best fit model to the Planck first year data combined with the WMAP polarization and high- ℓ CMB experiments [107]. We also show the anisotropy generated from the tensor mode with tensor to scalar ratio $r = 0.16$ which is recently suggested by the discovery of the BICEP2 experiment [8]. We use the publicly available CAMB code ¹ to compute the scalar and the tensor spectra. The ISW component can be easily calculated by the slight modification to the ‘*equations.f90*’. Most of the signal at $l > 20$ comes from the primary anisotropy while on large scales, significant fraction of anisotropy is generated at low redshifts, $z < 0.5$. We also show the first year low- ℓ Planck data ².

Because the large r value constrained by the B-mode power spectrum, C_l^{BB} of the BICEP2 enhances the amplitude of the temperature fluctuation, C_l^{TT} on large scales, it is required to make some modifications of the model to keep the current observational constraints from the WMAP or the Planck unchanged: either the smaller (i.e. negatively larger) value of running of scalar spectral index α_s [8] or isocurvature component of the initial fluctuation is required [67] to suppress the large scale power of the CMB temperature power spectrum. However, the amplitude of tensor mode with $r = 0.16$ model is subdominant at $\ell < 10$ compared to the ISW component. Thus there still remains some possibilities that the non-standard gravity models or the nonlinearity of the local large-scale structure can alter the amplitude of the ISW effect, and thus the constraint on the negatively large value of the running or the fraction of the isocurvature perturbation component might be reduced.

2.4. Non Linear ISW Effect

M. J. Rees and D. W. Sciama extended the Sachs-Wolfe calculation to non-linear collapsed objects in 1968 [113]. In 1967, they were investigating an apparent large-scale clustering of quasars [112] reported by Strittmatter & Faulkner [129]. They consider the possibility that inhomogeneity in the matter distribution inferred from the large-scale clustering of quasars creates anisotropy in the CMB as predicted by Sachs & Wolfe and estimates the amplitude of the temperature fluctuation induced by a spherically symmetric collapse of the objects in an expanding Universe [113]. Note that here we use the terminology of *non-linear* as the non-linear density fluctuations but the metric perturbations (hence the geodesic perturbations) are kept at the first order. The second order cosmological perturbation is treated in a consistent manner in [94, 134–136] but here we limit our discussion to the first order geodesic equation and non-linearity is only included in density perturbations. Using the Poisson equation, we see that there are two contributions to time evolution of a gravitational

¹ CAMB code is available at <http://camb.info/>

² Planck data can be retrieved from <http://www.esa.int/Planck>

potential

$$\Phi' = \frac{3}{2}\Omega_m \left(\frac{H_0}{k}\right)^2 \frac{1}{a} (i\mathbf{k} \cdot \mathbf{p} - \mathcal{H}\delta). \quad (21)$$

Here we have used the continuity equation $\delta' = i\mathbf{k} \cdot \mathbf{p}$, where \mathbf{p} is the momentum of the density field $\mathbf{p} = \mathbf{v}(1 + \delta)$. From equation (21), we see that the ISW and RS effects consist of two components: one proportional to the Hubble flow and the other the momentum of the object. In the linear perturbation limit, the momentum is equal to the velocity field so the linear ISW effect in principle traces the statistical property of the large-scale velocity field [22]. In a weakly non-linear regime or fully non-linear regime, a halo model approach is used to describe the non-linear time evolution of the gravitational potential which is originally developed for describing the non-linear clustering of the dark matter halo [22, 79, 120]. The dark matter power spectrum is described by the sum of two contributions: a two-halo term where the pair is in different halos, and a one-halo term where the pair is in the same halo [122]. Once we provide the mass function [e.g. 64, 125, 133, 142] and profile of the dark matter halo [89] then we can immediately calculate the non-linear clustering of the dark matter. Similarly, the velocity field can be decomposed into two components: the velocity due to the virial motion about the center of mass of its parent halo, and that due to the motion of the parent halo itself [124] which provides the non-linear momentum power spectrum [79].

Another approach is the higher order perturbation theory. As we will see in section 3, the cross correlation between the ISW and density tracer is useful to isolate the ISW effect from the CMB [24]. Then the angular cross correlation power spectrum between the ISW and any tracers of the density field can be some function of the cross power spectrum of Φ' and Φ ,

$$P_{\Phi'\Phi}(k) = \frac{9}{4}\Omega_m^2 \left(\frac{H_0}{k}\right)^4 \frac{1}{a^2} (P_{\delta\delta'} - \mathcal{H}P_{\delta\delta}), \quad (22)$$

where we employ the notation, $\langle X(\mathbf{k})Y^*(\mathbf{k}') \rangle \equiv (2\pi)^3 \delta^D(\mathbf{k} - \mathbf{k}') P_{XY}(k)$. The continuity equation is written as $\delta' = -\theta(1 + \delta)$ where θ is the divergence of the velocity. Then the perturbed variables δ and θ can be expanded in a series,

$$\delta(\mathbf{k}, \tau) = \sum_n D^n(\tau) \delta_n(\mathbf{k}, \tau), \quad (23)$$

$$\theta(\mathbf{k}, \tau) = \mathcal{H}f \sum_n D^n(\tau) \theta_n(\mathbf{k}, \tau), \quad (24)$$

where the n th variable is written in terms of a product of linear fluctuations as

$$\delta_n(\mathbf{k}, \tau) = \int \frac{d^3q_1}{(2\pi)^3} \cdots \frac{d^3q_n}{(2\pi)^3} \delta_1(\mathbf{q}_1) \cdots \delta_1(\mathbf{q}_n) F_n(\mathbf{q}_1, \cdots, \mathbf{q}_n) \delta^D\left(\sum_i \mathbf{q}_i - \mathbf{k}\right) \quad (25)$$

$$\theta_n(\mathbf{k}, \tau) = - \int \frac{d^3q_1}{(2\pi)^3} \cdots \frac{d^3q_n}{(2\pi)^3} \delta_1(\mathbf{q}_1) \cdots \delta_1(\mathbf{q}_n) G_n(\mathbf{q}_1, \cdots, \mathbf{q}_n) \delta^D\left(\sum_i \mathbf{q}_i - \mathbf{k}\right), \quad (26)$$

where δ^D is the Dirac delta function. The functions F_n and G_n describe the mode coupling between different wavevectors, and are explicitly given by [e.g. 63, 80]. Keeping all the terms which are less

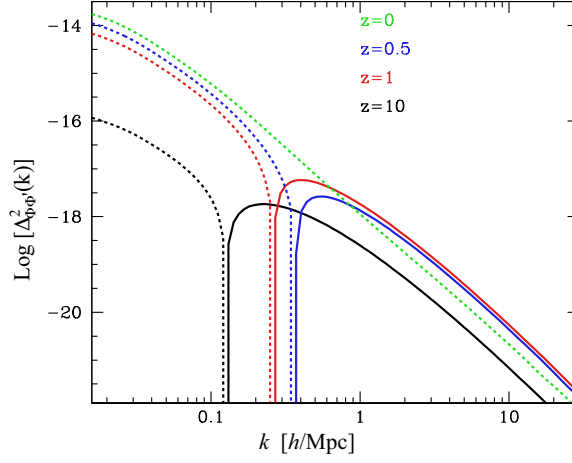


Fig. 2 The dimensionless cross power spectrum between Φ and Φ' , $\Delta_{\Phi\Phi'}^2(k)$ at different redshifts computed using equations (22), (27), and (28). Dashed lines show a negative cross power, while the solid lines positive. Figure is adapted from [91].

than fourth order of either δ_1 or θ_1 , we have [91]

$$P_{\delta\delta}(k) = D^2 P(k) + 2D^4 \int \frac{d^3q}{(2\pi)^3} P(q) [P(|\mathbf{k} - \mathbf{q}|) F_2^2(\mathbf{q}, \mathbf{k} - \mathbf{q}) + 3P(k) F_3(\mathbf{q}, -\mathbf{q}, \mathbf{k})], \quad (27)$$

$$\begin{aligned} P_{\delta\delta'}(k) = & \mathcal{H}f D^2 P(k) \\ & - \mathcal{H}f D^4 \left[P(k) \int \frac{d^3q}{(2\pi)^3} P(q) (F_3(\mathbf{q}, -\mathbf{q}, \mathbf{k}) + 3G_3(\mathbf{q}, -\mathbf{q}, \mathbf{k})) \right. \\ & + 2 \int \frac{d^3q}{(2\pi)^3} P(q) P(|\mathbf{k} - \mathbf{q}|) F_2^2(\mathbf{q}, \mathbf{k} - \mathbf{q}) G_2^2(\mathbf{q}, \mathbf{k} - \mathbf{q}) \\ & + 2 \int \frac{d^3q}{(2\pi)^3} \left(F_2(\mathbf{q}, \mathbf{k} - \mathbf{q}) P(q) P(|\mathbf{k} - \mathbf{q}|) + G_2(\mathbf{q}, \mathbf{q} - \mathbf{k}) P(k) P(|\mathbf{k} - \mathbf{q}|) \right. \\ & \left. \left. + F_2(\mathbf{k}, -\mathbf{q}) P(k) P(q) \right) \frac{\mathbf{k} \cdot \mathbf{q}}{q^2} \right], \quad (28) \end{aligned}$$

where $P(k)$ is the linear power spectrum of δ . More conveniently, $P_{\delta\delta'}$ can be approximated by $P_{\delta\delta'}(k, \tau) = \frac{1}{2} \frac{\partial}{\partial \tau} P_\delta(k, \tau)$ [93, 139].

Figure 2 shows the 3 dimensional cross correlation power spectrum of Φ and Φ' at different redshifts in Λ CDM Universe. In the linear regime, gravitational potential is negative $\Phi < 0$ in the overdense region and it decays with time due to the accelerating expansion so that $\Phi' > 0$. Thus Φ and Φ' show an anti-correlation. In the non linear regime, the gravitational potential grows, i.e. the potential well gets deeper thus $\Phi' < 0$ which gives Φ and Φ' a positive correlation. At redshift $z = 10$, the Universe is close to the matter dominated so that the linear ISW effect is small and the non-linear RS effect appears relatively prominently. At lower redshifts, the linear ISW effect is significantly enhanced since the fraction of dark energy becomes more substantial but we can still see the transition scale as the power turns from an anti-correlation to a correlation at $k \sim \mathcal{O}(0.1)$ Mpc/h. At $z = 0$, the linear ISW effect dominates at all scales.

The RS effect generates temperature anisotropy not only through the contraction and expansion of the structure but also the bulk motion of the structure perpendicular to the line of sight [3, 4, 86, 115].

Birkinshaw and Gull [9, 10] point out that the moving cluster which has transverse velocity to the line of sight may produce the local dipole structure on the CMB temperature. In order to explore the complete dynamics, N-body simulation with ray-tracing method is quite useful. Tuluie & Laguna [137, 138] carry out a ray tracing simulation for the maximum 360 Mpc/h box N-body simulation to see the cumulative temperature fluctuation from $z = 100$ to today. They separate the sources of anisotropy into the intrinsic change in gravitational potential of structure and the transverse bulk velocity of structure; however, the box size is not large enough to see the dynamics of clusters or voids whose sizes are larger than 100 Mpc/h. Cai et al. [20] use the Gigaparsec-size simulation to construct a full sky map of the ISW. They argue that the non-linear RS and moving halo contributions to the total are not significant, $< 10\%$ but the relative importance (relative to the linear ISW) is much higher if we go to higher redshift which is consistent with [19, 128] and with Figure 2. This is simply because the linear ISW is negligible at high redshifts where the Universe is still matter dominated, while the non-linear RS effect exists regardless of dark energy.

3. Observing the ISW and RS effects

The ISW effect is first detected in the CMB measured by the WMAP cross correlated with the large-scale structure data traced by the X-ray background radiation and radio galaxies [12]. Several attempts have been made to detect the ISW effect by cross correlating the CMB map measured by the COBE with the ROSAT X-ray background [68], NVSS radio galaxies [11] or HEAO1 X-ray background [14] but they could not detect the signal. However the non detection of the ISW effect can put an upper limit on the amount of dark energy and surprisingly Boughn & Crittenden [11] present the limit $\Omega_\Lambda < 0.74$ which is fairly close to the current limit of dark energy parameter [108]. Subsequently a number of papers appeared. Table 1 presents a summary of the detection of the ISW effect today. Some papers reach consistent conclusions while others show significant inconsistencies. It is mainly due to either the wrong statistics used or the contamination of the sample due to an incomplete subtraction of systematics.

In the following sub sections, we review the observations of the ISW and RS effects. In sec. 3.1, we define the cross correlation methods. In sec. 3.2, we discuss the possible systematic effects that affect the significance of the detection of the ISW effect.

3.1. Cross Correlation with LSS

Since the ISW effect is generated when photons pass through a time varying gravitational potential of the large-scale structure, it can be detected by cross correlating with some tracers of the large-scale structure. We can write this idea in the equation as

$$\langle \Theta \delta_{\text{LSS}} \rangle = \langle (\Theta_{\text{dec}} + \Theta_{\text{fg}} + \Theta_{\text{ISW}} + \Theta_{\text{SZ}} + \Theta_{\text{lens}} + \dots) \delta_{\text{LSS}} \rangle, \quad (29)$$

where Θ is a temperature fluctuation and δ_{LSS} is a density fluctuation of some tracers of the large-scale structure, e.g. galaxy number count. The sources of the CMB temperature fluctuation include: Θ_{dec} is the primary anisotropy at or before the decoupling epoch, and Θ_{fg} is any astrophysical foreground contamination from solar system or Galactic plane. The rest of the terms in equation (29) are attributed to the cosmological origin that generates secondary CMB anisotropy. Θ_{ISW} is the ISW effect, Θ_{SZ} is the Sunyaev-Zel'dovich (SZ) effect [130] and Θ_{lens} is the gravitational lens effect [44, 59, 72]. Here we assume that the large-scale structure is not correlated with the primary CMB at the decoupling epoch and we also assume that the ISW effect and the other secondary CMB

Author	CMB	LSS data	Redshift	Method	Detection	DE Constraints
Kneissl et al. '97 [68]	COBE4	ROSAT XRB	N/A	CCF	No detection	–
Boughn & Crittenden '98 [14]	COBE4	HEAO1 XRB	$z \simeq 1$	CCF	No detection	–
Boughn & Crittenden '02 [11]	COBE4	NVSS	$0 < z < 2$	CCF	No detection	$\Omega_\Lambda < 0.74$
Boughn & Crittenden '04,'05 [12, 13]	WMAP1	NVSS/HEAO1 XRB	$0 < z < 2$	CCF	$2-3\sigma$	–
Fosalba & Gaztanaga '04 [33]	WMAP1	APM	$z \simeq 0.15$	CCF	2.5σ	$\Omega_\Lambda = 0.8^{+0.06}_{-0.27}(2\sigma)$
Fosalba et al. '03 [34]	WMAP1	SDSS1(main, LRG) combined	$z \simeq 0.3, 0.5$	CCF	$2.0, 3.0\sigma$ 3.6σ	– $\Omega_\Lambda = 0.8^{+0.06}_{-0.11}(2\sigma)$
Scranton et al. '03 [119]	WMAP1	SDSS1(LRG)	$0.3 < z_p < 0.8$	CCF	$> 2\sigma$	–
Nolta et al. '04 [95]	WMAP1	NVSS	$0 < z < 2$	CCF	2.6σ	$\Omega_\Lambda = 0.68_{-0.68}(2.2\sigma)$
Afshordi et al. '04 [1]	WMAP1	2MASS	$0 < z < 0.2$	APS	2.5σ	–
Padmanabhan et al. '05 [97]	WMAP1	SDSS4(LRG)	$0.2 < z_p < 0.6$	APS	2.5σ	$\Omega_\Lambda = 0.8^{+0.05}_{-0.19}(2\sigma)$
Gaztanaga et al. '06 [37]	WMAP1	2MASS APM SDSS1(main,LRG) NVSS+HEAO	$z \sim 0.1$ $z \sim 0.15$ $z \sim 0.3, 0.5$ $z \sim 0.9$	CCF	4σ	$\Omega_\Lambda = 0.70^{+0.05}_{-0.17}(1\sigma)^a$ $w = -1.02^{+0.17}_{-0.17}(1\sigma)^a$
Cabre et al. '06 [18]	WMAP3	SDSS4(main, LRG)	$z \sim 0.3, 0.5$	CCF	4.4σ	$\Omega_\Lambda \simeq 0.83$
Giannantonio et al. '06 [39]	WMAP3	SDSS4(QSO)	$0.1 < z_p < 2.7$	CCF	$2 - 2.5\sigma$	$0.075 < \Omega_m < 0.475(1\sigma)$ $-1.18 < w < -0.76(1\sigma)$
Pietrobon et al. '06 [101]	WMAP3	NVSS	$0 < z < 2$	WLT	2.7σ	$0.41 < \Omega_\Lambda < 0.79(2\sigma)$
Vielva et al. '06 [141]	WMAP1	NVSS	$0 < z < 2$	WLT	3.3σ	$\Omega_\Lambda = 0.65^{+0.17}_{-0.20}(1\sigma)$ $w = -0.70^{+0.35}_{-0.50}(1\sigma)$
Rassat et al. '07 [111]	WMAP3	2MASS XSC	$0 < z < 0.2$	APS	$< 1\sigma$	$\Omega_\Lambda = 0.85^{+0.04}_{-0.18}(2\sigma)$
McEwen et al. '07 [84]	WMAP1	NVSS	$0 < z < 2$	WLT	$3.9\sigma^b$	$\Omega_\Lambda = 0.63^{+0.18}_{-0.17}(1\sigma)$ $w = -0.77^{+0.35}_{-0.36}(1\sigma)$
Giannantonio et al. '08, '12 [38, 42]	WMAP3,7	2MASS SDSS6,8(main) SDSS6,7(LRG) SDSS6(QSO) NVSS HEAO combined	$z \sim 0.2$ $z \simeq 0.3$ $z \simeq 0.5$ $0 < z < 3$ $0 < z < 2$ $0 < z < 2$	CCF	$0.5\sigma, 0.7\sigma$ $2.2\sigma, 2.2\sigma$ $2.2\sigma, 2.5\sigma$ $2.5\sigma, 2.3\sigma$ $3.3\sigma, 2.8\sigma$ $2.7\sigma, 2.4\sigma$ $4.5\sigma, 4.4\sigma$	$\Omega_m = 0.20^{+0.19}_{-0.11}(2\sigma)$
Raccanelli et al. '08 [110]	WMAP3	NVSS	$0 < z < 2$	CCF	2.5σ	–
McEwen et al. '08 [85]	WMAP3	NVSS	$0 < z < 2$	WLT	$\sim 3\sigma$	–
Ho et al. '08 [58]	WMAP3	2MASS SDSS(LRG) SDSS(QSO) NVSS combined	$0 < z < 0.2$ $0.2 < z_p < 0.6$ $0.5 < z < 2$ $0 < z < 3$	CCF	$0.2 - 1.4\sigma$ $1.3 - 2.5\sigma$ $0.2 - 1.4\sigma$ 2.9σ 3.7σ	$\Omega_\Lambda = 0.746^{+0.09}_{-0.09}(1\sigma)$
Granett et al. '08 [49]	WMAP5	SDSS6(LRG)	$0.4 < z_p < 0.75$	STK	4.4σ	–
Xia et al. '09 [145]	WMAP5	SDSS6(QSO)	$0 < z_p < 3$	CCF	$1.5 - 2.7\sigma$	$\Omega_m = 0.273^{+0.019}_{-0.019}(1\sigma)^c$
Hernandez-Monteagudo '10 [53]	WMAP5	NVSS	$0 < z < 3$	C/A	$\sim 2 - 3\sigma$	–
Sawangwit et al. '10 [117]	WMAP5	SDSS5 (LRG) 2SLAQ (LRG) AAO (LRG) NVSS	$0.2 < z_s < 0.5$ $0.4 < z_s < 0.7$ $0.5 < z_s < 0.9$ $0 < z < 2$	CCF	0.8σ 1.6σ 0.4σ $\sim 2\sigma$	– – – –
Lopez-Corredoira et al. '10 [76]	WMAP5	SDSS7		CCF	No detection	–
Francis & Peacock '10 [35]	WMAP3	2MASS XSC	$0 < z_p < 0.3$	APS	$\sim 1\sigma$	–
Goto et al. '12 [45]	WMAP7	WISE pre.	$0 < z < 0.3$	APS	$\sim 3\sigma$	–
Flender et al. '13 [32]	WMAP5	SDSS6 (LRG)	$0.4 < z_p < 0.75$	STK	$> 3\sigma$	–
Planck et al. XIX '13 [105]	Planck1	BOSS ^{d)} SDSS8(main) NVSS	$0 < z_s < 0.7$ $0.1 < z_p < 0.9$ $0 < z < 2$	C/A/W	1.7σ 2.0σ 2.9σ	– – –
Ilic et al. '13 [62]	WMAP7	SDSS6,7(Void)	$0 < z_s < 0.7$	STK	$\sim 3\sigma$	–
Hernandez-Monteagudo et al. '14 [54]	WMAP9	BOSS ^{d)}	$0.15 < z_p < 0.7$	C/A/W	$1.62 - 1.67\sigma$	–
Kovacs et al. '14 [71]	WMAP7	WISE full	$z \sim 0.15$	APS	$\sim 1.0\sigma$	–
Ferraro et al. '14 [31]	WMAP9	WISE full (gal) WISE full (AGN)	$z \sim 0.3$ $z \sim 1.1$	APS	$\sim 2.6\sigma$ $\sim 1.2\sigma$	– –

Table 1 The score sheet for the ISW detection. If the redshift of the large-scale structure tracer is measured spectroscopically, we denote the range with z_s . We use z_p for the range of photometric redshift, whereas we use z when the redshift is inferred by other methods like integrating the luminosity function, fitting the amplitude of cross correlation, or partial cross matching with the known redshift sources. The numbers after survey name stand for the data release, e.g. WMAP1 is the WMAP first-year data release, and SDSS4 is the SDSS fourth data release and so on. a) joint constraints with the Type Ia supernovae (SNIa) data. b) include a posteriori selection c) WMAP5+BAO+SNIa+ISW d) CMASS+LOWZ sample

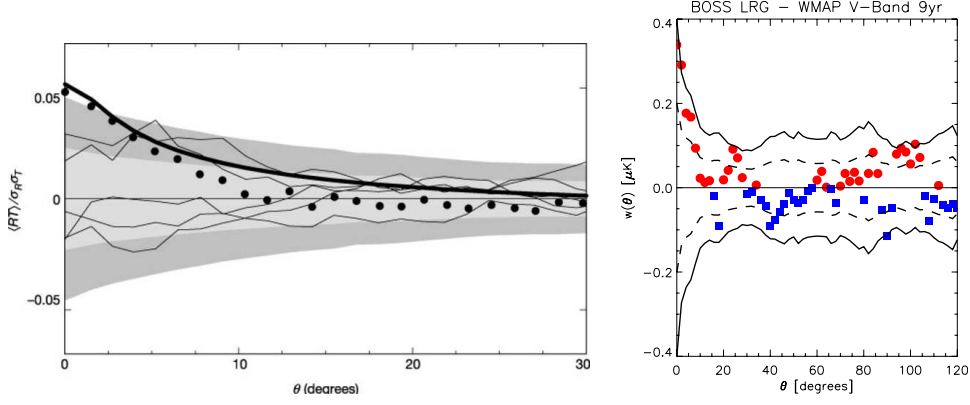


Fig. 3 Left panel shows the first detection of the ISW in 2004 by Boughe & Crittenden [12]. They use the WMAP first-year data cross correlated with the NVSS radio galaxies and X-ray data and find the ISW effect with 3.0σ detection. Right panel shows the latest detection in 2013 by Hernandez-Monteagudo et al. [54, but see also [31]]. They use the WMAP ninth-year data cross correlated with the LRG and CMASS galaxies observed by the BOSS and find the ISW effect with 1.6σ detection.

sources can be distinguished since the ISW effect is only important at largest scales while the other effects are dominant at much smaller scales.

3.1.1. Angular Power Spectrum. The observed quantities used in the literature can be classified into four: angular power spectrum, angular correlation function, wavelet and stacking. As we observe the CMB temperature fluctuation projected on the sky, it can be expanded into the spherical harmonic series

$$a_{lm}^{\text{ISW}} = \int d\Omega_{\hat{n}} \Theta_{\text{ISW}}(\hat{n}) Y_{lm}^*(\hat{n}), \quad (30)$$

where \hat{n} is a unit vector pointing toward a two dimensional position on the sky, Y_{lm} is the spherical harmonic function, $d\Omega_{\hat{n}}$ is a volume element of the unit sphere and the integral is over the whole sky.

The expanded temperature fluctuation can be cross correlated with the density tracer X ,

$$a_{lm}^X = \int d\Omega_{\hat{n}} \delta_X(\hat{n}) Y_{lm}^*(\hat{n}), \quad (31)$$

where X is the matter tracer field projected on to the sky by

$$\delta_X(\hat{n}) = \int_0^{r_*} dr \delta_m(\hat{n}r, \tau) W_X(r), \quad (32)$$

with the projection kernel W_X . The upper bound of the integral is defined by the maximum distance of the source that has a non-zero contribution to the projection. For the galaxy distribution, the projection kernel is,

$$W_{\text{gal}}(r) = b(r) r^2 \phi(r) \left[\int dr r^2 \phi(r) \right]^{-1} \quad (33)$$

where ϕ is the radial selection function and $b(r)$ is the galaxy bias which may depend on redshift but not on the scale (by assumption). We have assumed that in the scale where the ISW effect is important, the galaxy number counts are linearly related to the underlying dark matter density but strictly speaking the linear relation is valid only on very large scales. It breaks down on smaller

scales, introducing a possible source of systematics. However in most of the ISW studies it is typically enough to take into account the redshift evolution of the galaxy bias only and ignore a possible scale dependence of the bias. The weak lensing convergence is another powerful tool to trace the distribution of the dark matter, which has the kernel [see e.g. 6],

$$W_\kappa(r) = \frac{3}{2}\Omega_m H_0^2 \frac{r}{a} \int_r^{r_*} dr' p(r') \frac{r' - r}{r'}, \quad (34)$$

where $p(r)$ is the distribution of galaxies whose shapes are measured and it is normalized as $\int dr p(r) = 1$. From the statistical isotropy we can define the angular power spectrum (hereafter denoted as APS) as

$$\langle a_{lm}^{\text{ISW}} a_{l'm'}^{X*} \rangle = C_l^{\text{ISW-X}} \delta_{ll'} \delta_{mm'}. \quad (35)$$

Here the ensemble average is over possible realizations of the Universe ; however, we have only one Universe in reality. Thus C_l is estimated by averaging over $2l + 1$ modes for each multipole l -mode,

$$\hat{C}_l^{\text{ISW-X}} = \frac{1}{2l + 1} \sum_{m=-l}^{m=l} a_{lm}^{\text{CMB}} a_{lm}^{X*}. \quad (36)$$

In the practical observation, the whole sky is not observed. For example, we mask the region where the signal is not reliable or significantly contaminated by the foreground such as Galactic dust or synchrotron emission or zodiacal light of the solar system. The extra galactic radio sources should also be masked. Then the cut sky harmonic coefficient, \tilde{a}_{lm} , is given now

$$\tilde{a}_{lm} = \int d\Omega_{\hat{n}} W(\hat{n}) \Theta_{\text{ISW}}(\hat{n}) Y_{lm}^*(\hat{n}), \quad (37)$$

where $W(\hat{n})$ is a window function (or a mask function) that takes 1 at the observed pixel and 0 at the masked pixel. The power spectrum convolved with the mask function, $\tilde{C}_l \equiv \langle \tilde{a}_{lm} \tilde{a}_{lm}^* \rangle$ is called the Pseudo power spectrum. It has a smaller amplitude typically by $\tilde{C}_l \simeq f_{\text{sky}} C_l$ where f_{sky} is the fraction of sky observed. The effect of the mask can be corrected in an unbiased manner with the *Pseudo C_l estimator* (PCL) [29, 57], or *quadratic maximum likelihood estimator* (QML) [28, 131].

3.1.2. Angular Correlation Function. The cross correlation function (hereafter CCF) is defined as the Legendre transform of the power spectrum,

$$C^{\text{ISW-X}}(\theta) = \frac{1}{4\pi} \sum_l (2l + 1) C_l^{\text{ISW-X}} P_l(\cos \theta) b_l^{\text{CMB}} b_l^X p_l^2, \quad (38)$$

where p_l and b_l are the pixel and beam transfer functions, respectively. The inverse transform is

$$C_l^{\text{ISW-X}} = 2\pi \int d\cos \theta P(\cos \theta) C^{\text{ISW-X}}(\theta) (b_l^{\text{CMB}} b_l^X p_l^2)^{-1} \quad (39)$$

The estimator of the correlation function is nothing but

$$\hat{C}^{\text{ISW-X}}(\theta) \equiv \frac{\sum_{ij} \Theta_{\text{CMB}}(\hat{n}_i) \delta_X(\hat{n}_j) w_{\text{CMB}}(\hat{n}_i) w_X(\hat{n}_j)}{\sum_{ij} w_{\text{CMB}}(\hat{n}_i) w_X(\hat{n}_j)}, \quad (40)$$

where $\cos \theta = \hat{n}_i \cdot \hat{n}_j$. The function w is used to minimize the variance when the depth of the galaxy survey or effective sensitivity to the CMB at each pixel is not uniform, at the expense of increasing sample variance [33].

3.1.3. Wavelet. Wavelet analysis is useful particularly when signals are localized in both configuration and frequency space. For the cross correlation study the covariance of the wavelet coefficients (hereafter WLT) can be used [83, 101, 140, 141]. The WLT covariance at a given scale in configuration space R is defined as

$$C_{\Psi}^{\text{ISW-X}}(R) = \frac{1}{N_R} \sum_{\hat{\mathbf{n}}} \omega_{\text{CMB}}(R, \hat{\mathbf{n}}) \omega_X(R, \hat{\mathbf{n}}), \quad (41)$$

where $\omega(R, \hat{\mathbf{n}})$ is the wavelet coefficient at the position $\hat{\mathbf{n}}$. It can be obtained by convolving a map with a wavelet function. Here we assume that the wavelet function is given by a Spherical Mexican Hat (SMH) wavelet given by

$$\Psi(y, R) = \frac{1}{\sqrt{2\pi}N(R)} \left[1 + \left(\frac{y}{2} \right)^2 \right]^2 \left[2 - \left(\frac{y}{R} \right)^2 \right] e^{-y^2/2R^2}, \quad (42)$$

where $N(R)$ is a normalization constant, $N(R) = R\sqrt{1 + R^2/2 + R^4/4}$. The distance on the tangent plane is given by $y = 2 \tan(\theta/2)$. Then the WLT coefficient is,

$$\omega_X(R, \hat{\mathbf{n}}) = \int d\Omega_{\hat{\mathbf{n}}'} X(\hat{\mathbf{n}} - \hat{\mathbf{n}}') \Psi(\theta', R), \quad (43)$$

where the volume element $d\Omega_{\hat{\mathbf{n}}}$ subtends an infinitesimal solid angle pointing toward $\hat{\mathbf{n}} = (\theta, \phi)$. The observed WLT covariance can be compared with the theoretical calculation with this formula,

$$C_{\Psi}^{\text{ISW-X,TH}}(R) = \sum_l \frac{2l+1}{4\pi} p_l^2 \Psi_l^2(R) b_l^{\text{CMB}} b_l^X C_l^{\text{ISW-X,TH}}, \quad (44)$$

where Ψ_l is the spherical harmonic coefficient of the SMH and $C_l^{\text{ISW-X,TH}}$ is the theoretical prediction of the cross correlation APS between the ISW and mass tracer.

The choice of the wavelet function, equation (42), is not unique. Veilva et al. 2004 and Mukherjee & Wnag 2004 [88, 140] applied SMH wavelet and Cruz et al. 2006 [25] used the elliptical Mexican Hat wavelet to find a prominent cold spot in the CMB map with more than 2σ . However, Zhang & Huterer 2010 [147] claimed that the cold spot is found to be statistically significant only if the SMH wavelet is used, but not with the tophat or Gaussian windows. As we mentioned the WLT is useful for finding localized features in the data while we should be careful for interpreting the results, given the degree of freedom in choosing the wavelet functions.

3.1.4. Stacking. A stacking method is particularly useful for measuring the average temperature profile of the CMB around clusters and voids [21, 49, 50, 62, 105] and for finding the correspondence between the temperature fluctuation and the specific structure of the density field [49, 55, 98, 99]. The stacked CMB temperature can be expressed as

$$S(R) = \sum_i^n A_i^{-1} \int d\Omega_i \Delta T(\phi_i, \theta_i) M(\phi_i, \theta_i) \Xi(\theta_i, R) \quad (45)$$

where the normalization is $A_i = \int d\Omega M(\phi_i, \theta_i)$, M is the composite mask of the CMB and large-scale structure, and Ξ is the filter function. For the compensated filter that eliminates the constant offset of the temperature, the filter function is given as [see e.g. 21, 92],

$$\Xi(\theta_i, R) = \begin{cases} 1, & \theta_i < R \\ -1, & R \leq \theta_i < \cos^{-1}(2 \cos R - 1) \\ 0, & \text{otherwise} \end{cases} \quad (46)$$

Here we take a local coordinate system in which the z-axis is pointing to the i -th cluster or void center with θ_i, ϕ_i and $d\Omega_i$ denoting the polar and azimuthal angles and the volume element in this

local coordinate systems, respectively. The radius R is the physical scale instead of the angle which satisfies the relation $R = \varphi_i \chi(z_i)$ where φ_i is the angle that subtends the size of a cluster or a void lying at a comoving distance $\chi(z_i)$. In other words the CMB temperature profile is rescaled before stacking, which increases the statistical significance of the correlation signal [62, 92]. Stacking the CMB at the locations of clusters and voids gives a typical profile of the CMB temperature. Since the sign of the ISW temperature fluctuation is opposite at the voids and clusters, we take the difference between the stacked temperature at voids and clusters, i.e.

$$S(R) = S_{\text{cluster}}(R) - S_{\text{void}}(R). \quad (47)$$

The interpretation of the significance of the detection of the ISW with the stacking analysis needs careful treatment. As pointed out in Ref [55], if we look at the particular scale, the significance is prominent and have tension to the standard Λ CDM prediction but the significance goes down if we combine all scales; it is so called a posteriori selection effect [7, 55, 62, 105].

3.2. systematic errors

As seen in table 1, the reported detection significances vary among papers and are often not consistent with each other, even if they use the same CMB and large-scale structure data sets. It is partly because of the difference in the statistics they used and partly because of the imperfect control of the systematics. In this section, we discuss possible contamination which may affect the analysis of the ISW effect. The main contaminant of the CMB is foreground Galactic dust and synchrotron emissions. On the other hand, the galaxy distribution as a tracer of the large-scale structure has also uncertainty including the incomplete star-galaxy separation, magnification bias, and redshift distribution uncertainties. Furthermore, the SZ effect and point source contamination can be a source of systematics which is discussed in the later section.

3.2.1. Magnification bias. Suppose that we correlate the CMB with the number count of galaxies. The observed number count of galaxies reflects the true, underlying clustering of galaxies, while it can also generate an apparent (artificial) clustering in the sky due to various effects. The gravitational lens effect alters the number count of galaxies through two effects. It locally changes the area of the sky observed hence the number of galaxies observed. It also magnifies the light of the distant faint galaxies, and thus enhances the number of galaxies observed in the vicinity of massive low- z galaxies [e.g. 15]. Given that we observe the galaxy number density at a certain redshift bin, z_i , the observed number density can be written as a sum of two components, [77],

$$\delta_{\text{gal}}^{\text{obs}}(\hat{\mathbf{n}}, z_i) = \delta_{\text{gal}}^{\text{s}}(\hat{\mathbf{n}}, z_i) + \delta_{\text{gal}}^{\mu}(\hat{\mathbf{n}}, z_i), \quad (48)$$

where $\delta_{\text{gal}}^{\text{s}}$ is the intrinsic galaxy or, in other words, unlensed galaxy number density and $\delta_{\text{gal}}^{\mu}$ is the magnification bias correction. Now we make a modification to the equation (33). The underlying three dimensional dark matter fluctuations projected into a redshift bin z_i with the kernel is,

$$\delta_{\text{gal}}^{\text{s}}(\hat{\mathbf{n}}, z_i) = \int dz b(z) W^{\text{s}}(z, z_i) \delta_{\text{m}}[\hat{\mathbf{n}}\chi(z)], \quad (49)$$

where $b(z)$ is a galaxy bias which depends on redshift and $W^{\text{s}}(z, z_i)$ is a kernel that projects galaxies at z onto a redshift bin of z_i . The explicit form of the kernel depends on the model assumed. If we assume that each galaxy has a redshift measured with a Gaussian error of $\sigma(z)$, the kernel can be

written as

$$W^s(z, z_i) = \frac{1}{2}N(z) \left[\operatorname{erfc} \left(\frac{(i-1)\Delta_z - z}{\sqrt{2}\sigma(z)} \right) - \operatorname{erfc} \left(\frac{i\Delta_z - z}{\sqrt{2}\sigma(z)} \right) \right], \quad (50)$$

where Δ_z is the width of the redshift bin, erfc is the complementary error function and $N(z)$ is redshift distribution of galaxies which satisfies, $N(z)dz = p(r)dr = r^2\phi(r)dr$ normalized as $\int dz N(z) = 1$.

Now we derive the expression of δ_{gal}^μ . The gravitational lens deflects light and thus changes the position of galaxies as

$$\hat{\mathbf{n}}^s = \hat{\mathbf{n}} + \delta\hat{\mathbf{n}}, \quad (51)$$

where the superscript s denotes the quantity for unlensed galaxies, and $\delta\hat{\mathbf{n}}$ is deflection angle. The magnification can be given by the Jacobian of the mapping of $\hat{\mathbf{n}}^s \rightarrow \hat{\mathbf{n}}$: i.e.

$$A^{-1} \equiv \left| \frac{\partial \hat{\mathbf{n}}^s}{\partial \hat{\mathbf{n}}} \right|. \quad (52)$$

The galaxy flux is magnified by

$$f = Af^s, \quad (53)$$

where f is the observed flux and f^s is the intrinsic galaxy flux. In the weak lensing limit, the magnification can be approximated as $A \approx 1 + 2\kappa$, where κ is the so-called ‘‘convergence field’’, which satisfies $|\kappa| \ll 1$. In this limit, the observed number density of galaxies can be expressed in terms of the number density of unlensed galaxies as,

$$\delta_{\text{gal}}^{\text{obs}}(\hat{\mathbf{n}}, z) = \delta_{\text{gal}}^s(\hat{\mathbf{n}} + \delta\hat{\mathbf{n}}, z) + (5\alpha(z) - 2)\kappa[1 + \delta_{\text{gal}}^s(\hat{\mathbf{n}} + \delta\hat{\mathbf{n}}, z)], \quad (54)$$

where α is the logarithmic slope of the cumulative number counts of galaxies at the faint end

$$\alpha = \left. \frac{d \log N(> m)}{dm} \right|_{m_{\text{lim}}}. \quad (55)$$

This definition of α is only true for galaxy populations that have a linear slope in the relation between the logarithmic cumulative number and the magnitude. Though in most cases it is true, one can generalize the definition of α by introducing an efficiency function [61]. In the weak lensing limit, the deflection angle $\delta\hat{\mathbf{n}}$ is also a first order small quantity. Expanding $\delta_{\text{gal}}^s(\hat{\mathbf{n}} + \delta\hat{\mathbf{n}})$ and keeping the first order term gives

$$\delta_{\text{gal}}^{\text{obs}}(z, \hat{\mathbf{n}}) = \delta_{\text{gal}}^s(z, \hat{\mathbf{n}}) + (5\alpha - 2)\kappa, \quad (56)$$

where the second term of the RHS denotes the $\delta_{\text{gal}}^\mu(z, \hat{\mathbf{n}})$. Using the expression of the convergence κ for the sources distributed around the z_i bin, we obtain

$$\delta_{\text{gal}}^\mu(\hat{\mathbf{n}}, z_i) = \frac{3\Omega_m H_0^2}{2} (5\alpha(z_i) - 2) \int \frac{dz}{H(z)} g(z, z_i) (1+z) \delta_m[\hat{\mathbf{n}}\chi(z)], \quad (57)$$

where χ is the comoving distance and the lensing efficiency function g is given by

$$g(z, z_i) = \chi(z) \int_z^\infty dz' \frac{\chi(z') - \chi(z)}{\chi(z')} W(z', z_i). \quad (58)$$

It has been shown that the magnification bias in the ISW analysis does not affect the constraints on dark energy parameters inferred from low- z samples; however, it can have a significant impact when we cross-correlate the CMB with galaxy samples at $z > 2$ [77]. Thus, we need to be careful when interpreting the null detection of the ISW at high redshift.

3.2.2. Extinctions. The Galactic dust extinction may be a major source of systematics in the measurement of the ISW effect [38, 42]. In the region where the Galactic dust extinction is high, the galaxy colors tend to be red and alter the large-scale distribution of the galaxy sample depending on the wavelength observed. In the high extinction region, we also expect the observed temperature map to contain microwave emission from the Galactic dust which then produce a spurious correlations between the temperature map and the galaxy count data. The advantages to use the near- to mid-infrared are to minimize the amount of the dust extinction, which enables us to mitigate the systematics. Correcting the effect of dust is essential for the cross-correlation study because it allows us to use more sky area. As the ISW effect appears only on large angular scales where both the CMB and galaxy data are almost sample variance limited, increasing the usable sky area is the only way to increase statistical significance of the cross-correlation signal. [43, 102–104, 118, 146]. However the dust correction contains uncertainty and it may affect the precise measurement. A more conservative approach is to simply mask out the contaminated region of the sky. Giannantonio et al. [41] exclude the high extinction region with $A_r > 0.18$ and 0.08 which leaves the usable sky fraction of $f_{\text{sky}} = 0.22$ and 0.11 , respectively. The latter has less contamination but larger statistical error and is statistically consistent with the former to within 1σ . Therefore the former cut appears to be sufficient for this data set.

3.2.3. SZ and point sources. A correlation between the CMB and the large-scale structure is also generated by the SZ effect and point sources. As high energy electron scatters CMB photon through the inverse Compton scattering in a high temperature cluster of galaxies, the SZ effect distorts the shape of the blackbody CMB spectrum. For that reason, the temperature change induced by the SZ effect depends on the frequency we observe; temperature decreases at low frequency while it increases at high frequency and no change occurs at 217 GHz. Thus the SZ signal in the cross correlation can in principle be isolated with multi-frequency observations. Furthermore, the characteristic angular scale that the SZ effect correlates with the large-scale structure is smaller than that of the ISW effect. In the harmonics space, the ISW peaks at $l = 2$ and becomes negligible at $l = 30$ while the SZ effect becomes important at $l > 100$ [1, 56, 119]. The point sources found in the CMB map are extra-galactic sources such as AGNs and dusty galaxies. They are bright in low (AGNs) and high (dusty galaxies) frequency bands. They are also visible in optical and infrared bands, where many galaxy survey data are available. They also produce a correlation between the CMB and large-scale structure; however, it can be distinguished from the ISW signal because point sources produce a correlation at much smaller scales than that of the ISW effect [1, 30, 60]. This discrimination by scale is possible only for the power spectrum in harmonics space but impossible for the correlation function in the configuration space because, in the harmonic space, multipole scales where ISW and point sources signals become prominent are different while in the configuration space, different angular scales and the different physical origins do not have one to one correspondence [53, 54]. Although the point sources can be removed by masking if they are resolved by CMB experiments, unresolved galaxies may still bring an extra-correlation signal.

4. Application to the Cosmology

4.1. Constraints On Dark Energy in Λ - and w -CDM model

As first pointed out by Crittenden & Turok 1996 [24], the ISW effect can be used as a powerful probe of dark energy. In this section we describe the background Universe by the flat FRW metric with matter and generalized time varying dark energy. Then we can write the Friedmann equation

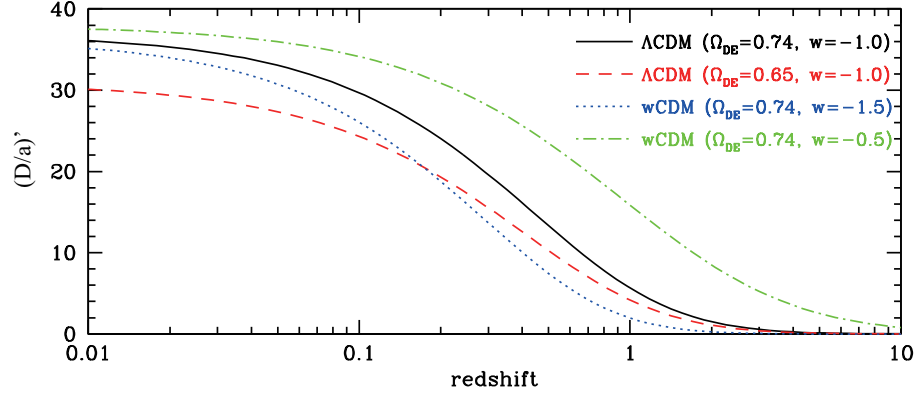


Fig. 4 Dependence of the ISW effect on the cosmological models, $(D/a)'$, as a function of redshift is shown. The less amount of dark energy makes Universe more close to the EdS, and thus produces weaker ISW effect (black solid and red dashed). Less negative equation of state, w (green dot-dashed) makes dark energy dominate at earlier epoch and enhances the ISW effect. That model can be tested by the cross correlation with high- z objects like QSOs or radio galaxies.

as

$$H^2(z) = H_0^2[\Omega_m(1+z)^3 + \Omega_{DE}\zeta(z, w)], \quad (59)$$

where the function ζ is given by

$$\zeta(z, w) = \exp \left[3 \int_0^z dz' \frac{1 + w(z')}{1 + z'} \right], \quad (60)$$

where w is in general a function of redshift but it is parametrized as $w = \text{const.}$ or $w(z) = w_0 + w_a \frac{z}{1+z}$ where w_0 and w_a are constants [e.g. 75]. The explicit cosmological dependence of the ISW effect originates from $\partial_\tau(D/a) = \mathcal{H}D(f-1)$ and the matter power spectrum. When we combine other cosmological data sets such as galaxy clustering or weak lensing, the ISW effect provides information on dark energy via $\mathcal{H}D(f-1)$ term. This quantity is shown in Figure 4 as a function of redshift. Less amount of dark energy makes Universe more close to the EdS Universe, and thus produces weaker ISW effect (the black solid and the red dashed lines). Larger value of equation of state, i.e. $w > -1$ (the green dot-dashed line), makes dark energy prominent at earlier time which enhances the ISW effect. Such an early dark energy models can be tested by the cross correlation with the high- z density tracers like quasars, which lie at $z < 3$ [114].

Table 1 shows the summary of reported detections of the ISW effect and the constraints on dark energy models. Boughn and Crittenden 2002 [11] put the first constraint on dark energy parameter by cross-correlating the NVSS galaxies number counts with the CMB temperature observed by the COBE. Although they do not find a significant detection of the ISW effect, it gives an upper limit of the amount of dark energy, $\Omega_\Lambda < 0.74$. The redshift distribution of the NVSS galaxies is inferred from an integral of a luminosity function of the radio galaxies [27]. With the inferred redshift distribution, the galaxy auto-correlation power spectrum can nicely account for the observed clustering of the radio galaxies but it is not sufficient to validate the true redshift distribution. Fosalba & Gaztanaga 2004 [33] present more stringent constraints on the Λ CDM model with the APM galaxy survey and the WMAP data. They fixed the Hubble parameter, σ_8 and the constant bias parameter

with assuming a flat geometry and obtained $0.53 < \Omega_\Lambda < 0.86$ (2σ). Fosalba et al. 2003 [34] find similar result from the combined analysis of the APM galaxies, the SDSS main galaxies and the LRG sample, $0.69 < \Omega_\Lambda < 0.87$ (2σ). They utilize the cross-correlation function for the measurement of the ISW effect. The covariance matrix is estimated in two ways: a Jack Knife resampling and a Monte Carlo simulation. The Jack Knife (JK) error is consistent with the Monte Carlo (MC) on large scales while the JK error is significantly under-estimated on scales smaller than $\theta < 2$ degrees. Nolte et al. 2004 [95] revisit the NVSS cross correlation with the WMAP. Thanks to the greater sensitivity of the WMAP, they find the 2.6σ detection of the ISW effect with CCF, and obtain the constraint of $\Omega_\Lambda > 0$ at 2σ . They also reject the closed Universe at 3σ significance in which the ISW signal shows a negative cross correlation with the large-scale structure. The covariance matrix is estimated by the MC simulations for randomly generated CMB spectra, while keeping large-scale structure unchanged. This may underestimate the error since the large-scale structure and primary CMB as well as the cross correlation between them all contribute to the covariance matrix as shown in equation (62).

For a joint analysis of the ISW and the galaxy clustering APS, the logarithm of the likelihood function, $\chi^2 \equiv -2 \ln \mathcal{L}$, is given by

$$\chi^2 = (x_{\text{obs}}^i - \langle x^i \rangle) [\mathbf{C}^{-1}]_{ij} (x_{\text{obs}}^j - \langle x^j \rangle), \quad (61)$$

where x_{obs} is the observed APS, C_l^{gT} , and the index i represents both the angular l -bin and sample used, when we use multiple samples for the large-scale structure tracers. The covariance matrix \mathbf{C} can be estimated in different ways. The Fisher matrix formalism gives the theoretical estimate of the covariance matrix, while the Jack Knife (JK) or the bootstrap (BS) resampling give the estimate of the covariance based on the observational data itself. The latter tends to underestimate the true error due to the lack of the modes larger than the survey volume. The Monte Carlo simulation is particularly useful when the data are not Gaussian, or the processes such as complicated radial or angular selection functions are taken into account. For the Gaussian case, the covariance matrix can be simply calculated by the Fisher formula,

$$\mathbf{C} = \frac{1}{f_{\text{sky}}(2l+1)} [\tilde{C}_l^{\text{g}} \tilde{C}_l^{\text{gT}} + (C_l^{\text{gT}})^2], \quad (62)$$

where \tilde{C}^{g} is the power spectrum of the galaxies with the shot noise, $\tilde{C}_l^{\text{g}} = C_l^{\text{g}} + \bar{n}_g^{-1}$ where n_g is the number density of galaxies and $\tilde{C}_l^{\text{T}} = C_l^{\text{T}} + N_l^{\text{T}}$ where N_l^{T} is the noise power spectrum of the CMB. Padmanabhan et al. 2005 [97] use the fourth data release of the SDSS LRG photometric sample with accurate photometric redshifts $\Delta z_p = 0.03$. The cross-correlation APS is used as an estimator and they introduce a quadratic estimator [121, 131] which enables us a nearly maximum likelihood estimation. Gaztanaga et al. 2006 [37] explore Λ CDM model with multiple large-scale structure tracers: 2MASS, APM, SDSS, NVSS and HEAO. They point out that the parameter degeneracy between Ω_Λ and Ω_m obtained from the ISW effect is perpendicular to those from SNIa observation and thus the combination of the ISW effect with other cosmological probes can be a powerful tool to constrain those parameters. Combining the ISW data with the SNIa data, they obtain the cosmological constraints of $\Omega_\Lambda = 0.7 \pm 0.05$ and $w = -1.02 \pm 0.17$. Using the same data set, Corasaniti et al. 2005 [23] extend the analysis to constraining the model where dark energy has clustering with a finite sound speed but do not find a meaningful constraint on the sound speed of dark energy. Some works [84, 101, 141] use wavelet for constraining dark energy models. As we mentioned before, the wavelet analysis has the advantage of detecting localized signals. Therefore, it

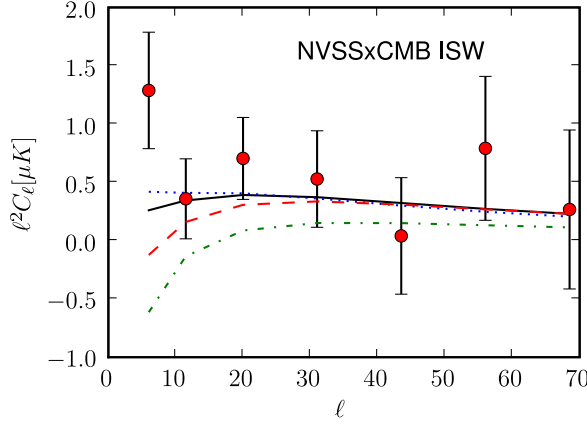


Fig. 5 The cross correlation power spectrum of the ISW and NVSS galaxy. The lines show the best fit f_{NL} model (black solid), $f_{NL} = 100$ (blue dotted), $f_{NL} = -100$ (red dashed), and $f_{NL} = 800$ (green dot-dashed) while keeping the other cosmological parameters unchanged. The figure is adopted from Slosar et al. 2008 [126].

has the higher significance than other method in terms of the signal to noise ratio of finding a signal at a given scale [141]. They find the signal of the ISW effect with higher significance of $\sim 3\sigma$ than other methods. The error covariance for the wavelet is derived in a straightforward manner using equations (44) and (62),

$$\Delta \left[C_{\Psi}^{\text{ISW-X,TH}}(R) \right]^2 = \sum_l \frac{2l+1}{16\pi^2} p_l^4 \Psi_l^4(R) (b_l^{\text{CMB}} b_l^{\text{X}})^2 \left[C_l^{\text{CMB}} C_l^{\text{X}} + \left(C_l^{\text{ISW-X}} \right)^2 \right]. \quad (63)$$

They present consistent results with the current Ω_{Λ} constraint [e.g. 107] but slightly lower values are favored. The equation of state parameter favors larger (less negative) value but it is still consistent with a cosmological constant within 1σ level.

4.2. Non Gaussianity

Although the recent observation of the CMB by the Planck shows that the non Gaussianity (NG) of the primordial fluctuation is consistent with zero, it is still worth discussing it for the future observations which would give much tighter constraints on (or potentially detect) NG. In this section, we describe the possible impacts of the NG of the primordial fluctuation on the ISW effect. We assume that the NG has the form of [36, 70],

$$\Phi = \phi + f_{NL}(\phi^2 - \langle \phi^2 \rangle) \quad (64)$$

with the parameter f_{NL} which describes the amplitude of NG of the primordial fluctuation, and ϕ is a random Gaussian variable.

The ISW effect basically plays two roles in the context of NG. First, the ISW effect can be a proxy of mass of the large-scale structure especially on large scales. It is difficult to discriminate the primordial NG from those which originate from the non linear gravitational evolution of the structure. However, the non-zero f_{NL} alters the number of rare objects formed responding to the initial gravitational potentials. The number of rare objects is enhanced if the f_{NL} is positive but depressed for the negative f_{NL} . Thus the effect of non-zero f_{NL} on the halo or galaxy power spectrum becomes

prominent on large scales [26]. As a result, the NG bias acquires a correction of $b \rightarrow b + \Delta b$, where

$$\Delta b(k) = 2(1 - b)f_{\text{NL}}\delta_c \frac{3\Omega_m H_0^2}{2D(a)k^2}, \quad (65)$$

where δ_c is the critical density, b is the usual Eulerian constant bias. Thus the NG can be constrained through the ISW-galaxy cross correlation. The galaxy-galaxy auto-correlation is mainly used for constraining the NG and the ISW-galaxy cross correlation has relatively lower statistical power. However, the cross correlation is less sensitive to the systematic effects and thus gives a robust measurement; they are complementary to each other. Figure 5 compares the cross correlation power spectrum of the ISW and the NVSS galaxies with the standard Λ CDM prediction and NG predictions keeping all the parameters other than f_{NL} unchanged [126]. Slosar et al. 2008 [126] found no significant detection of the NG. They obtained a constraint of $f_{\text{NL}} = 105^{+647}_{-337}$ from using only the ISW-NVSS cross correlation, while Afshordi & Tolley 2008 [2] found a 2σ hint for the NG, $f_{\text{NL}} = 236 \pm 127$. Xia et al. 2011 [144] also found a weak evidence for the positive f_{NL} , $f_{\text{NL}} = 74 \pm 40(1\sigma)$ by combining the auto correlation of the NVSS and the NVSS-ISW cross correlation. They used the redshift distribution of the NVSS galaxies which was directly measured by the limited number of spectroscopic galaxies [16] whereas Slosar et al. 2008 [126] used one measured from the NVSS clustering itself, which made significant difference in the f_{NL} . Lately Giannantonio et al. 2014 [41] point out that the NVSS catalog contains a serious systematic error: the number density of galaxies depends on declination and right ascension. This systematics largely affects auto correlation of the NVSS galaxies while the impact of the systematics on the cross correlation is small. Giannantonio and Percival 2014 [40] revisit the NG constraints via cross correlation of the ISW effect with a suite of galaxy samples and find no evidence of the NG, $f_{\text{NL}} = 46 \pm 68$ by using the ISW-galaxy cross correlation only. They also take into account the cross correlation of the CMB-lensing with galaxy samples and obtain a joint constraint of $f_{\text{NL}} = 12 \pm 21$ in the end. This is consistent with the CMB bispectrum analysis of the Planck [109].

Second, the ISW effect may bring a systematic effect to the measurement of the CMB bispectrum through the ISW-lensing correlation [44, 109]. The observed CMB temperature can be decomposed into three parts; primordial CMB at last scattering surface, lensed-CMB, and the secondary anisotropy that is generated at low redshifts such as the ISW or the SZ. For the Gaussian field, all the information is encoded into the power spectrum or two point correlation function so that the bispectrum or three point function is the lowest statistics that describes the NG clustering. However, the ISW effect and the CMB-lensing are correlated with each other because the large-scale structure that makes CMB photon deflect via gravitational lens also induces the ISW effect at low redshift. Therefore it mimics the primordial NG to produce a non-zero signal in the CMB bispectrum. The ISW effect is important on large scales and the CMB-lensing appears on much smaller scales, so the ISW-lensing bispectrum peaks at a squeezed configuration of the triangle. Thus the correlation between the CMB-lens and the ISW effect brings a bias on the measurement of the primordial NG especially for the local type by $\Delta f_{\text{NL}} \simeq 10$ [20, 69] which may seriously affect the current measurement; i.e. $\sigma_{f_{\text{NL}}} = 5.8$ [109]. On the other hand, the ISW-lensing bias to the other configurations of the bispectrum is negligible [52, 65, 81, 82, 123, 127].

5. Summary

In this article we review the ISW effect induced by linear and non-linear structures of the Universe. It is well known that the Sachs-Wolfe effect and the ISW effect are simultaneously derived from

the cosmological perturbation theory. The ISW effect can be generated by scalar, vector and tensor mode fluctuations of the metric but the significant contribution comes from the scalar mode, which is related to the time variation of the matter density fluctuation. The recent detection of the tensor-mode CMB polarization claimed by the BICEP2 collaboration [8] can indeed be the polarization generated by the tensor-mode ISW effect from primordial gravitational waves. The time variation of the gravitational potential in the standard Λ CDM Universe comes from: 1) the coherent decay of the gravitational potential due to the accelerating expansion of the Universe, 2) the isotropic clustering inflow of mass lump toward the center of mass, and 3) the transverse motions of the clusters. The latter two effects are too tiny to detect with the current CMB experiments but it might be possible to detect with future experiments having finer angular resolutions such as ACTPol [90], SPTPol [5] or COrE [132].

We also review the observational studies of the ISW effect. The ISW effect was first detected by the cross correlation of the CMB observed by the WMAP with the number counts of the radio galaxies measured by the NVSS. The significance of detection was $2 - 3\sigma$ [12]. Subsequently a number of detections have been reported with various tracers of dark matter using a variety of statistical methods. As the ISW effect reflects the large-scale fluctuations in the Universe, they can be used for constraining the cosmological models especially at low redshifts ($z < 1$). The statistical error of the ISW effect is mostly dominated by sample variance but the detection significances vary among papers and are often not consistent with each other. It is partly due to the consequence of the different statistics they used, different treatments of the foreground, or different estimates or assumptions on the redshift distribution of galaxies. As we acquire more knowledge on those issues, we may be able to understand inconsistencies seen in table 1. All sky polarization data from the Planck will be useful for further studying the dust model of our Galaxy as well as the confirmation of the large amplitude of tensor mode fluctuation discovered by the BICEP2. In addition to this, complete BOSS spectroscopic galaxies and QSOs samples can be used for calibrating the redshift distribution of galaxies and QSOs. Therefore both the Planck and the BOSS data which are going to be delivered soon would allow us to extensively study the ISW effect with better understandings of the systematics.

acknowledgement

The author would like to thank Eiichiro Komatsu for the careful reading of this article and giving many useful comments. This work is supported in part by the FIRST program "Subaru Measurements of Images and Redshifts (SuMRe)" initiated by the Council for Science and Technology Policy (CSTP).

References

- [1] N. Afshordi, Y.-S. Loh, and M. A. Strauss, Phys. Rev. D, **69**(8), 083524 (April 2004).
- [2] N. Afshordi and A. J. Tolley, Phys. Rev. D, **78**(12), 123507 (December 2008).
- [3] N. Aghanim, S. Prunet, O. Forni, and F. R. Bouchet, Astronomy & Astrophysics, **334**, 409–419 (June 1998).
- [4] O. Aso, M. Hattori, and T. Futamase, ApJL, **576**, L5–L7 (September 2002).
- [5] J. E. Austermann, K. A. Aird, J. A. Beall, D. Becker, A. Bender, B. A. Benson, L. E. Bleem, J. Britton, et al., SPT-pol: an instrument for CMB polarization measurements with the South Pole Telescope, In *Society of Photo-Optical Instrumentation Engineers (SPIE) Conference Series*, volume 8452 of *Society of Photo-Optical Instrumentation Engineers (SPIE) Conference Series* (September 2012).
- [6] M. Bartelmann and P. Schneider, Phys.Rep., **340**, 291–472 (January 2001).
- [7] C. L. Bennett, R. S. Hill, G. Hinshaw, D. Larson, K. M. Smith, J. Dunkley, B. Gold, M. Halpern, et al., ApJS, **192**, 17 (February 2011).
- [8] BICEP2 Collaboration, P. A. R Ade, R. W. Aikin, D. Barkats, S. J. Benton, C. A. Bischoff, J. J. Bock, J. A. Brevik,

- and et al., ArXiv 1403.3985 (March 2014).
- [9] M. Birkinshaw, Moving Gravitational Lenses, In J. M. Moran, J. N. Hewitt, and K.-Y. Lo, editors, *Gravitational Lenses*, volume 330 of *Lecture Notes in Physics*, Berlin Springer Verlag, page 59 (1989).
 - [10] M. Birkinshaw and S. F. Gull, *Nature*, **302**, 315–317 (March 1983).
 - [11] S. P. Boughn and R. G. Crittenden, *Physical Review Letters*, **88**(2), 021302 (January 2002).
 - [12] S. P. Boughn and R. G. Crittenden, *Nature*, **427**, 45–47 (January 2004).
 - [13] S. P. Boughn and R. G. Crittenden, *New Astron. Rev.*, **49**, 75–78 (May 2005).
 - [14] S. P. Boughn, R. G. Crittenden, and N. G. Turok, *New Astron.*, **3**, 275–291 (July 1998).
 - [15] T. J. Broadhurst, A. N. Taylor, and J. A. Peacock, *ApJ*, **438**, 49–61 (January 1995).
 - [16] M. H. Brookes, P. N. Best, J. A. Peacock, H. J. A. Röttgering, and J. S. Dunlop, *MNRAS*, **385**, 1297–1326 (April 2008).
 - [17] E. F. Bunn and N. Sugiyama, *ApJ*, **446**, 49 (June 1995).
 - [18] A. Cabré, E. Gaztañaga, M. Manera, P. Fosalba, and F. Castander, *MNRAS*, **372**, L23–L27 (October 2006).
 - [19] Y.-C. Cai, S. Cole, A. Jenkins, and C. Frenk, *MNRAS*, **396**, 772–778 (June 2009).
 - [20] Y.-C. Cai, S. Cole, A. Jenkins, and C. S. Frenk, *MNRAS*, **407**, 201–224 (September 2010).
 - [21] Y.-C. Cai, M. C. Neyrinck, I. Szapudi, S. Cole, and C. S. Frenk, ArXiv 1301.6136 (January 2013).
 - [22] A. Cooray and R. Sheth, *Phys.Rep.*, **372**, 1–129 (December 2002).
 - [23] P.-S. Corasaniti, T. Giannantonio, and A. Melchiorri, *Phys. Rev. D*, **71**(12), 123521 (June 2005).
 - [24] R. G. Crittenden and N. Turok, *Physical Review Letters*, **76**, 575–578 (January 1996).
 - [25] M. Cruz, M. Tucci, E. Martínez-González, and P. Vielva, *MNRAS*, **369**, 57–67 (June 2006).
 - [26] N. Dalal, O. Doré, D. Huterer, and A. Shirokov, *Phys. Rev. D*, **77**(12), 123514 (June 2008).
 - [27] J. S. Dunlop and J. A. Peacock, *MNRAS*, **247**, 19 (November 1990).
 - [28] G. Efstathiou, *MNRAS*, **348**, 885–896 (March 2004).
 - [29] G. Efstathiou, *MNRAS*, **349**, 603–626 (April 2004).
 - [30] H. K. Eriksen, G. Huey, R. Saha, F. K. Hansen, J. Dick, A. J. Banday, K. M. Górski, P. Jain, and et al., *ApJ*, **656**, 641–652 (February 2007).
 - [31] S. Ferraro, B. D. Sherwin, and D. N. Spergel, ArXiv 1401.1193 (January 2014).
 - [32] S. Flender, S. Hotchkiss, and S. Nadathur, *JCAP*, **2**, 13 (February 2013).
 - [33] P. Fosalba and E. Gaztañaga, *MNRAS*, **350**, L37–L41 (May 2004).
 - [34] P. Fosalba, E. Gaztañaga, and F. J. Castander, *ApJL*, **597**, L89–L92 (November 2003).
 - [35] C. L. Francis and J. A. Peacock, *MNRAS*, **406**, 2–13 (July 2010).
 - [36] A. Gangui, F. Lucchin, S. Matarrese, and S. Mollerach, *ApJ*, **430**, 447–457 (August 1994).
 - [37] E. Gaztañaga, M. Manera, and T. Multamäki, *MNRAS*, **365**, 171–177 (January 2006).
 - [38] T. Giannantonio, R. Crittenden, R. Nichol, and A. J. Ross, *MNRAS*, **426**, 2581–2599 (November 2012).
 - [39] T. Giannantonio, R. G. Crittenden, R. C. Nichol, R. Scranton, G. T. Richards, A. D. Myers, R. J. Brunner, A. G. Gray, and et al., *Phys. Rev. D*, **74**(6), 063520 (September 2006).
 - [40] T. Giannantonio and W. J. Percival, *MNRAS*, in press (ArXiv 1312.5154) (March 2014).
 - [41] T. Giannantonio, A. J. Ross, W. J. Percival, R. Crittenden, D. Bacher, M. Kilbinger, R. Nichol, and J. Weller, *Phys. Rev. D*, **89**(2), 023511 (January 2014).
 - [42] T. Giannantonio, R. Scranton, R. G. Crittenden, R. C. Nichol, S. P. Boughn, A. D. Myers, and G. T. Richards, *Phys. Rev. D*, **77**(12), 123520 (June 2008).
 - [43] B. Gold, N. Odegard, J. L. Weiland, R. S. Hill, A. Kogut, C. L. Bennett, G. Hinshaw, X. Chen, and et al., *ApJS*, **192**, 15 (February 2011).
 - [44] D. M. Goldberg and D. N. Spergel, *Phys. Rev. D*, **59**(10), 103002 (May 1999).
 - [45] T. Goto, I. Szapudi, and B. R. Granett, *MNRAS*, **422**, L77 (May 2012).
 - [46] N. Gouda and N. Sugiyama, *ApJL*, **395**, L59–L63 (August 1992).
 - [47] N. Gouda, N. Sugiyama, and M. Sasaki, *ApJL*, **372**, L49–L52 (May 1991).
 - [48] N. Gouda, N. Sugiyama, and M. Sasaki, *Progress of Theoretical Physics*, **85**, 1023–1039 (May 1991).
 - [49] B. R. Granett, M. C. Neyrinck, and I. Szapudi, *ApJL*, **683**, L99–L102 (August 2008).
 - [50] B. R. Granett, M. C. Neyrinck, and I. Szapudi, *ApJ*, **701**, 414–422 (August 2009).
 - [51] A. J. S. Hamilton, *MNRAS*, **312**, 257–284 (February 2000).
 - [52] D. Hanson, K. M. Smith, A. Challinor, and M. Liguori, *Phys. Rev. D*, **80**(8), 083004 (October 2009).
 - [53] C. Hernández-Monteagudo, *Astronomy & Astrophysics*, **520**, A101 (September 2010).
 - [54] C. Hernández-Monteagudo, A. J. Ross, A. Cuesta, R. Génova-Santos, J.-Q. Xia, F. Prada, G. Rossi, M. Neyrinck, and et al., *MNRAS*, **438**, 1724–1740 (February 2014).
 - [55] C. Hernández-Monteagudo and R. E. Smith, *MNRAS*, **435**, 1094–1107 (October 2013).
 - [56] J. C. Hill and D. N. Spergel, ArXiv 1312.4525 (December 2013).
 - [57] E. Hivon, K. M. Górski, C. B. Netterfield, B. P. Crill, S. Prunet, and F. Hansen, *ApJ*, **567**, 2–17 (March 2002).
 - [58] S. Ho, C. Hirata, N. Padmanabhan, U. Seljak, and N. Bahcall, *Phys. Rev. D*, **78**(4), 043519 (August 2008).
 - [59] W. Hu, *Phys. Rev. D*, **62**(4), 043007 (August 2000).
 - [60] K. M. Huffenberger, H. K. Eriksen, and F. K. Hansen, *ApJL*, **651**, L81–L84 (November 2006).

-
- [61] L. Hui, E. Gaztañaga, and M. Loverde, *Phys. Rev. D*, **76**(10), 103502 (November 2007).
 - [62] S. Ilić, M. Langer, and M. Douspis, *Astronomy & Astrophysics*, **556**, A51 (August 2013).
 - [63] B. Jain and E. Bertschinger, *ApJ*, **431**, 495–505 (August 1994).
 - [64] A. Jenkins, C. S. Frenk, S. D. M. White, J. M. Colberg, S. Cole, A. E. Evrard, H. M. P. Couchman, and N. Yoshida, *MNRAS*, **321**, 372–384 (February 2001).
 - [65] V. Junk and E. Komatsu, *Phys. Rev. D*, **85**(12), 123524 (June 2012).
 - [66] N. Kaiser and A. Stebbins, *Nature*, **310**, 391–393 (August 1984).
 - [67] M. Kawasaki, T. Sekiguchi, T. Takahashi, and S. Yokoyama, *ArXiv* 1404.2175 (April 2014).
 - [68] R. Kneissl, R. Egger, G. Hasinger, A. M. Soltan, and J. Truemper, *Astronomy & Astrophysics*, **320**, 685–695 (April 1997).
 - [69] E. Komatsu, *Classical and Quantum Gravity*, **27**(12), 124010 (June 2010).
 - [70] E. Komatsu and D. N. Spergel, *Phys. Rev. D*, **63**(6), 063002 (March 2001).
 - [71] A. Kovács and I. Szapudi, *ArXiv* 1401.0156 (December 2014).
 - [72] A. Lewis and A. Challinor, *Phys.Rep.*, **429**, 1–65 (June 2006).
 - [73] A. R. Liddle and D. H. Lyth, *Phys.Rep.*, **231**, 1–105 (August 1993).
 - [74] A. R. Liddle and D. H. Lyth, *Cosmological Inflation and Large-Scale Structure*, June 2000).
 - [75] E. V. Linder, *Physical Review Letters*, **90**(9), 091301 (March 2003).
 - [76] M. López-Corredoira, F. Sylos Labini, and J. Betancort-Rijo, *Astronomy & Astrophysics*, **513**, A3 (April 2010).
 - [77] M. Loverde, L. Hui, and E. Gaztañaga, *Phys. Rev. D*, **75**(4), 043519 (February 2007).
 - [78] C.-P. Ma and E. Bertschinger, *ApJ*, **455**, 7 (December 1995).
 - [79] C.-P. Ma and J. N. Fry, *Physical Review Letters*, **88**(21), 211301 (May 2002).
 - [80] N. Makino, M. Sasaki, and Y. Suto, *Phys. Rev. D*, **46**, 585–602 (July 1992).
 - [81] A. Mangilli and L. Verde, *Phys. Rev. D*, **80**(12), 123007 (December 2009).
 - [82] A. Mangilli, B. Wandelt, F. Elsner, and M. Liguori, *Astronomy & Astrophysics*, **555**, A82 (July 2013).
 - [83] E. Martínez-González, J. E. Gallegos, F. Argüeso, L. Cayón, and J. L. Sanz, *MNRAS*, **336**, 22–32 (October 2002).
 - [84] J. D. McEwen, P. Vielva, M. P. Hobson, E. Martínez-González, and A. N. Lasenby, *MNRAS*, **376**, 1211–1226 (April 2007).
 - [85] J. D. McEwen, Y. Wiaux, M. P. Hobson, P. Vanderghenst, and A. N. Lasenby, *MNRAS*, **384**, 1289–1300 (March 2008).
 - [86] S. M. Molnar and M. Birkinshaw, *ApJ*, **537**, 542–554 (July 2000).
 - [87] V. F. Mukhanov, H. A. Feldman, and R. H. Brandenberger, *Phys.Rep.*, **215**, 203–333 (June 1992).
 - [88] P. Mukherjee and Y. Wang, *ApJ*, **613**, 51–60 (September 2004).
 - [89] J. F. Navarro, C. S. Frenk, and S. D. M. White, *ApJ*, **490**, 493 (December 1997).
 - [90] M. D. Niemack, P. A. R. Ade, J. Aguirre, F. Barrientos, J. A. Beall, J. R. Bond, J. Britton, H. M. Cho, et al., ACTPol: a polarization-sensitive receiver for the Atacama Cosmology Telescope, In *Society of Photo-Optical Instrumentation Engineers (SPIE) Conference Series*, volume 7741 of *Society of Photo-Optical Instrumentation Engineers (SPIE) Conference Series* (July 2010).
 - [91] A. J. Nishizawa, Ph.D. Thesis (March 2008).
 - [92] A. J. Nishizawa and K. T. Inoue, in preparation (2014).
 - [93] A. J. Nishizawa, E. Komatsu, N. Yoshida, R. Takahashi, and N. Sugiyama, *ApJL*, **676**, L93–L96 (April 2008).
 - [94] H. Noh and J.-C. Hwang, *Phys. Rev. D*, **69**(10), 104011 (May 2004).
 - [95] M. R. Nolta, E. L. Wright, L. Page, C. L. Bennett, M. Halpern, G. Hinshaw, N. Jarosik, A. Kogut, and et al., *ApJ*, **608**, 10–15 (June 2004).
 - [96] J. P. Ostriker and E. T. Vishniac, *ApJL*, **306**, L51–L54 (July 1986).
 - [97] N. Padmanabhan, C. M. Hirata, U. Seljak, D. J. Schlegel, J. Brinkmann, and D. P. Schneider, *Phys. Rev. D*, **72**(4), 043525 (August 2005).
 - [98] P. Pápai and I. Szapudi, *ApJ*, **725**, 2078–2086 (December 2010).
 - [99] P. Pápai, I. Szapudi, and B. R. Granett, *ApJ*, **732**, 27 (May 2011).
 - [100] A. A. Penzias and R. W. Wilson, *ApJ*, **142**, 419–421 (July 1965).
 - [101] D. Pietrobon, A. Balbi, and D. Marinucci, *Phys. Rev. D*, **74**(4), 043524 (August 2006).
 - [102] Planck Collaboration, P. A. R. Ade, N. Aghanim, M. I. R. Alves, C. Armitage-Caplan, M. Arnaud, M. Ashdown, F. Atrio-Barandela, J. Aumont, C. Baccigaluppi, and et al., *ArXiv* 1303.5073 (March 2013).
 - [103] Planck Collaboration, P. A. R. Ade, N. Aghanim, M. I. R. Alves, M. Arnaud, M. Ashdown, F. Atrio-Barandela, J. Aumont, C. Baccigaluppi, A. J. Banday, and et al., *ArXiv* 1307.6815 (July 2013).
 - [104] Planck Collaboration, P. A. R. Ade, N. Aghanim, C. Armitage-Caplan, M. Arnaud, M. Ashdown, F. Atrio-Barandela, J. Aumont, C. Baccigaluppi, A. J. Banday, and et al., *ArXiv* 1303.5072 (March 2013).
 - [105] Planck Collaboration, P. A. R. Ade, N. Aghanim, C. Armitage-Caplan, M. Arnaud, M. Ashdown, F. Atrio-Barandela, J. Aumont, C. Baccigaluppi, A. J. Banday, and et al., *ArXiv* 1303.5079 (March 2013).
 - [106] Planck collaboration, P. A. R. Ade, N. Aghanim, C. Armitage-Caplan, M. Arnaud, M. Ashdown, F. Atrio-Barandela, J. Aumont, C. Baccigaluppi, A. J. Banday, and et al., *ArXiv* 1303.5075 (March 2013).

-
- [107] Planck Collaboration, P. A. R. Ade, N. Aghanim, C. Armitage-Caplan, M. Arnaud, M. Ashdown, F. Atrio-Barandela, J. Aumont, C. Baccigalupi, A. J. Banday, and et al., ArXiv 1303.5076 (March 2013).
 - [108] Planck Collaboration, P. A. R. Ade, N. Aghanim, C. Armitage-Caplan, M. Arnaud, M. Ashdown, F. Atrio-Barandela, J. Aumont, C. Baccigalupi, A. J. Banday, and et al., ArXiv 1303.5077 (March 2013).
 - [109] Planck Collaboration, P. A. R. Ade, N. Aghanim, C. Armitage-Caplan, M. Arnaud, M. Ashdown, F. Atrio-Barandela, J. Aumont, C. Baccigalupi, A. J. Banday, and et al., ArXiv 1303.5084 (March 2013).
 - [110] A. Raccanelli, A. Bonaldi, M. Negrello, S. Matarrese, G. Tormen, and G. de Zotti, MNRAS, **386**, 2161–2166 (June 2008).
 - [111] A. Rassat, K. Land, O. Lahav, and F. B. Abdalla, MNRAS, **377**, 1085–1094 (May 2007).
 - [112] M. J. Rees and D. W. Sciama, Nature, **213**, 374–375 (January 1967).
 - [113] M. J. Rees and D. W. Sciama, Nature, **217**, 511–516 (February 1968).
 - [114] N. P. Ross, A. D. Myers, E. S. Sheldon, C. Yèche, M. A. Strauss, J. Bovy, J. A. Kirkpatrick, G. T. Richards, and et al., ApJS, **199**, 3 (March 2012).
 - [115] J. A. Rubiño-Martín, C. Hernández-Monteagudo, and T. A. Enßlin, Astronomy & Astrophysics, **419**, 439–447 (May 2004).
 - [116] R. K. Sachs and A. M. Wolfe, ApJ, **147**, 73 (January 1967).
 - [117] U. Sawangwit, T. Shanks, R. D. Cannon, S. M. Croom, N. P. Ross, and D. A. Wake, MNRAS, **402**, 2228–2244 (March 2010).
 - [118] D. J. Schlegel, D. P. Finkbeiner, and M. Davis, ApJ, **500**, 525 (June 1998).
 - [119] R. Scranton, A. J. Connolly, R. C. Nichol, A. Stebbins, I. Szapudi, D. J. Eisenstein, N. Afshordi, T. Budavari, and et al., ArXiv astro-ph/0307335 (July 2003).
 - [120] U. Seljak, ApJ, **460**, 549 (April 1996).
 - [121] U. Seljak, ApJ, **506**, 64–79 (October 1998).
 - [122] U. Seljak, MNRAS, **318**, 203–213 (October 2000).
 - [123] P. Serra and A. Cooray, Phys. Rev. D, **77**(10), 107305 (May 2008).
 - [124] R. K. Sheth and A. Diaferio, MNRAS, **322**, 901–917 (April 2001).
 - [125] R. K. Sheth and G. Tormen, MNRAS, **308**, 119–126 (September 1999).
 - [126] A. Slosar, C. Hirata, U. Seljak, S. Ho, and N. Padmanabhan, JCAP, **8**, 31 (August 2008).
 - [127] K. M. Smith and M. Zaldarriaga, MNRAS, **417**, 2–19 (October 2011).
 - [128] R. E. Smith, C. Hernández-Monteagudo, and U. Seljak, Phys. Rev. D, **80**(6), 063528 (September 2009).
 - [129] P. Strittmatter and J. Faulkner, Nature, **212**, 1441–1442 (December 1966).
 - [130] R. A. Sunyaev and Y. B. Zeldovich, Astrophys. & Space Science, **7**, 3–19 (April 1970).
 - [131] M. Tegmark, Phys. Rev. D, **55**, 5895–5907 (May 1997).
 - [132] The CORe Collaboration, C. Armitage-Caplan, M. Avilez, D. Barbosa, A. Banday, N. Bartolo, R. Battye, J. Bernard, et al., ArXiv 1102.2181 (February 2011).
 - [133] J. L. Tinker, B. E. Robertson, A. V. Kravtsov, A. Klypin, M. S. Warren, G. Yepes, and S. Gottlöber, ApJ, **724**, 878–886 (December 2010).
 - [134] K. Tomita, Phys. Rev. D, **72**(10), 103506 (November 2005).
 - [135] K. Tomita, Phys. Rev. D, **72**(4), 043526 (August 2005).
 - [136] K. Tomita and K. T. Inoue, Phys. Rev. D, **77**(10), 103522 (May 2008).
 - [137] R. Tuluie and P. Laguna, ApJL, **445**, L73–L76 (June 1995).
 - [138] R. Tuluie, P. Laguna, and P. Anninos, ApJ, **463**, 15 (May 1996).
 - [139] L. Verde and D. N. Spergel, Phys. Rev. D, **65**(4), 043007 (February 2002).
 - [140] P. Vielva, E. Martínez-González, R. B. Barreiro, J. L. Sanz, and L. Cayón, ApJ, **609**, 22–34 (July 2004).
 - [141] P. Vielva, E. Martínez-González, and M. Tucci, MNRAS, **365**, 891–901 (January 2006).
 - [142] M. S. Warren, K. Abazajian, D. E. Holz, and L. Teodoro, ApJ, **646**, 881–885 (August 2006).
 - [143] D. T. Wilkinson and R. B. Partridge, Nature, **215**, 719 (August 1967).
 - [144] J.-Q. Xia, C. Baccigalupi, S. Matarrese, L. Verde, and M. Viel, JCAP, **8**, 33 (August 2011).
 - [145] J.-Q. Xia, M. Viel, C. Baccigalupi, and S. Matarrese, JCAP, **9**, 3 (September 2009).
 - [146] K. Yahata, A. Yonehara, Y. Suto, E. L. Turner, T. Broadhurst, and D. P. Finkbeiner, PASJ, **59**, 205–219 (February 2007).
 - [147] R. Zhang and D. Huterer, Astroparticle Physics, **33**, 69–74 (March 2010).